

MEASUREMENT OF  
ELASTIC ELECTRON-NEUTRON SCATTERING AND  
INELASTIC ELECTRON-DEUTERON SCATTERING CROSS  
SECTIONS AT HIGH MOMENTUM TRANSFER\*

S. Rock,\* R. G. Arnold,\* P. E. Bosted,\* B. T. Certok,† B. A. Mecking,°  
I. Schmidt,‡ Z. M. Szalata,\* R. C. York,° and R. Zdarko<sup>▷,\*</sup>

<sup>▷</sup>Stanford Linear Accelerator Center  
Stanford University, Stanford, CA 94309  
and

\*The American University, Washington, DC 20016

ABSTRACT

We have measured inelastic electron-deuteron, electron-proton, and electron-aluminum cross sections at  $10^\circ$  in the kinematic region between elastic deuteron scattering and the second resonance region at six beam energies between 9.8 and 21 GeV. The elastic electron-neutron cross section was extracted from the quasi-elastic data at  $Q^2 = 2.5, 4.0, 6.0, 8.0$  and  $10.0$   $(\text{GeV}/c)^2$ . The ratio of elastic cross sections  $\sigma_n/\sigma_p$  falls with increasing  $Q^2$  above  $6$   $(\text{GeV}/c)^2$ . The inelastic data are compatible either with  $y$ -scaling (scattering from a single nucleon) or with  $\xi$  scaling (scattering from quarks).

Submitted to *Physical Review D*

---

\* Work supported in part by Department of Energy contract DE-AC03-76SF00515 and by National Science Foundation grants PHY78-09378 and PHY85-10549.

† Deceased

Current Addresses:

° CEBAF, Newport News, VA.

‡ University Technica Federico Santa Maria, Valparaiso, Chile.

° University of Virginia, Charlottesville, VA.

## I. INTRODUCTION

We have measured the elastic electron-neutron cross section  $d\sigma_n/d\Omega$  at momentum transfers squared ( $Q^2$ ) of 2.5, 4.0, 6.0, 8.0, and 10.0  $(\text{GeV}/c)^2$  at a laboratory angle of  $10^\circ$ . These were extracted from cross sections measured over the entire quasi-elastic peak and into the resonance region on deuterium, hydrogen, and aluminum targets. In addition, inelastic cross sections were measured from deuterium and aluminum targets near the kinematics for electron-deuteron elastic scattering.

The elastic electron-nucleon cross sections have been calculated by a wide variety of empirical and theoretical models, ranging from Form Factor Scaling [1] and Vector Meson Dominance (VMD) [2-6] to Quark-Parton models [7,8] and perturbative QCD [9]. Hybrid models [10] using VMD at low  $Q^2$  and perturbative QCD at high  $Q^2$  have also been proposed. The effects of the soft nucleon wave function [11] for intermediate values of  $Q^2$  have also been estimated. At large enough  $Q^2$  the Quark Dimensional Scaling Laws [12] predict that the form factors decrease as  $Q^{2n}$  where  $n$  depends on the number of quark constituents ( $n = 2$  for the nucleon); then the ratio of neutron-to-proton elastic cross sections depends on the quark wave functions inside the nucleons. Different assumptions on the wave function symmetries result in different predictions on the neutron to proton ratio at asymptotically large  $Q^2$ .

The entire spectrum of electron-scattering cross sections on nuclei—including deep inelastic, the quasi-elastic and the very high Bjorken  $x$  [13,14] region near the elastic electron-nucleus kinematics—have generated great theoretical and experimental interest. This includes results on the  $y$ -scaling [15-17] of quasi-elastic nuclei cross sections, the EMC effect [18] at medium and low values of  $x$ , and the large ratio of heavy target to deuterium cross sections at  $x > 1$  [19].

## A. Kinematics

The elastic electron-nucleon cross section in the one-photon exchange approximation is given by

$$\sigma^{\text{el}} \equiv \frac{d\sigma}{d\Omega} = \sigma_{\text{Mott}} \left[ \frac{G_E^2(Q^2) + \tau G_M^2(Q^2)}{(1 + \tau)} + 2\tau G_M^2(Q^2) \tan^2\left(\frac{\Theta}{2}\right) \right] \quad (1)$$

where  $Q^2 = 4EE' \sin^2(\Theta/2)$  is the four-momentum transfer squared;  $E$  is the incoming electron energy,  $\Theta$  is the electron scattering angle,  $E'$  is the scattered electron energy in the lab rest frame;  $\tau = Q^2/(4M_p^2)$ ;  $M_p$  is the proton mass;  $\sigma_{\text{Mott}} = \alpha^2/\{4E^2 \sin^4(\Theta/2)[1 + (2E/M_p) \sin^2(\Theta/2)]\}$  and  $G_E(Q^2)$  and  $G_M(Q^2)$  are the electric and magnetic form factors. The two form factors are often expressed in terms of the Dirac and Pauli form factors,  $F_1 = (\tau G_M + G_E)/(1 + \tau)$  and  $F_2 = (G_M - G_E)/(1 + \tau)$ . At small angles, the ratio

$$\frac{\sigma_n^{\text{el}}}{\sigma_p^{\text{el}}} = \frac{(F_{1n}^2 + \tau F_{2n}^2)}{(F_{1p}^2 + \tau F_{2p}^2)} = \frac{(G_{En}^2 + \tau G_{Mn}^2)}{(G_{Ep}^2 + \tau G_{Mp}^2)}. \quad (2)$$

The inelastic electron-nucleon differential cross section in the one-photon exchange approximation can be written as

$$\frac{d^2\sigma}{d\Omega dE'} = \sigma_{NS} \left[ W_2(x, Q^2) + 2W_1(x, Q^2) \tan^2\left(\frac{\Theta}{2}\right) \right], \quad (3)$$

where  $W_2$  and  $W_1$  are the inelastic structure functions;  $x = Q^2/(2M_p\nu)$  is the Bjorken scaling variable;  $\nu = E - E'$ ; and  $\sigma_{NS} = \alpha^2/[4E^2 \sin^4(\Theta/2)]$  is the Non-structure cross section.

In the limit of elastic scattering, the inelastic structure functions become

$$W_1^{\text{el}}(x, Q^2) = \frac{Q^2}{4M_p^2} G_M^2(Q^2) \delta(2M_p\tau - \nu)$$

and

$$W_2^{\text{el}}(x, Q^2) = \frac{G_E^2(Q^2) + \tau G_M^2(Q^2)}{1 + \tau} \delta(2M_p\tau - \nu).$$

For quasi-elastic scattering, the  $\delta$  functions are replaced by Gaussian-like peaks.

## B. Experimental Method

Electrons which scattered from either a hydrogen, deuterium, or aluminum target were detected in the SLAC 20-GeV spectrometer [20,21] set at  $\theta = 10.00^\circ$ . Overlapping spectra of scattered electron momentum distributions were measured in a region covering the entire quasi-elastic peak and into the resonance region. To reduce systematic uncertainties in ratios of cross sections, the spectrometer momentum was changed in steps of 1% and at each setting cross sections were measured using the hydrogen, deuterium and dummy aluminum targets. Several such sweeps were done to further reduce possible systematic uncertainties due to long time scale instabilities.

In the impulse approximation, the scattering from deuterium occurs from either the proton or the neutron, with the other nucleon being a spectator. The initial Fermi momentum of the struck nucleon is described by the deuteron wave function. When the target nucleon is moving inside the nucleus the elastic kinematical relation between  $E, E'$  and  $\Theta$  no longer holds and thus the reconstructed missing mass

$$W^2 = M_p^2 + 2M_p(E - E') - 4EE' \sin^2 \frac{\Theta}{2} \quad (4)$$

of the recoil nucleon has a Gaussian-like distribution around  $W^2 = M_p^2$ . The full-width at half-maximum of this Fermi-smeared quasi-elastic peak is about  $\delta E'/E' \sim 3\%$  at the kinematics of this experiment. Figure 1 shows a Monte Carlo simulation of the quasi-elastic peak including the radiative effects as a function of  $W^2$ . The peak is wider at higher  $Q^2$  due to the kinematic relation between  $W^2$  and  $E'$ . The missing mass spectrum is similarly smeared for inelastic scattering from the moving nucleons. The spectrum observed is the sum of elastic and inelastic scattering from the moving nucleons. For small angles, the width of the quasi-elastic peak in  $W^2$  increases approximately as  $\sqrt{Q^2}$ . The ratio of elastic-to-inelastic cross section

decreases with increasing  $Q^2$ . Thus the relative size of the quasi-elastic peak becomes smaller with increasing  $Q^2$ . This determines the upper limit of  $Q^2$  for which we can measure elastic-neutron scattering.

The elastic neutron cross section ( $\sigma_n^{\text{el}}$ ) is extracted from the deuteron cross section ( $\sigma_d$ ) using the proton elastic ( $\sigma_p^{\text{el}}$ ) and inelastic ( $\sigma_p^{\text{in}}$ ) cross sections. The proton cross sections are ‘smeared’ by using models of the deuteron wave function, and then compared with the experimental deuteron spectrum. The excess signal is due to scattering from the neutron. By comparing cross sections from deuterium and hydrogen taken in the same spectrometer, many systematic uncertainties in acceptance, beam monitoring, etc., will cancel. Details of the procedure are given in Section 3.

The rest of the paper is divided as follows. Section 2 describes the experimental equipment. Section 3 describes the analysis and results from the proton elastic peak calibration, the quasi-elastic spectra, the elastic neutron cross section, the aluminum cross section and the threshold region.

## 2. EXPERIMENTAL EQUIPMENT

### A. Beam

The SLAC electron beam with incident energies between 9.761 and 21.001 GeV, typical beam pulse length of 1.6  $\mu\text{s}$ , and repetition rates of up to 210 Hz were used. Figure 2 shows the elements of the beam and detector system. The beam passed through the A-bend momentum-defining magnets and slits before entering End Station A. Table I shows the beam parameters.

The beam intensity was measured by two toroidal charge monitors. These were periodically calibrated by passing a precisely known charge through calibration windings while the electron beam was off. The toroids were periodically compared

with the charge measurements from a Faraday cup, which could be inserted in the beam line. The two toroids agreed with each other and with the Faraday cup to better than 0.5%. This led to the systematic uncertainties shown in Table II. These uncertainties partly cancel in the ratio of cross sections.

The beam position was monitored periodically using two fluorescent screens located approximately 2 m and 12 m upstream of the target. The position of the beam on these screens could be estimated within  $\pm 1$  mm, producing an uncertainty on the incident angle of the beam of approximately  $\pm 0.2$  mr. Since the elastic cross section varies approximately as  $\theta^{-12}$ , this results in a systematic error of  $\pm 1.4\%$  on the cross section. This partly cancels in the ratio of cross sections, as shown in Table II.

The beam energy was determined by energy-defining slits that were set at values between 0.25% and 0.4% Full Width, as shown in Table I. Previous experiments [22], and more recent experiments [23] using the same beam transport line have cited an overall calibration uncertainty of  $\pm 0.1\%$ . Since the elastic cross section varies as  $\sim E^{-10}$ , this results in a systematic uncertainty of 1.0%. The uncertainty cancels in the cross section ratios. In addition, the beam energy can drift around its central value. These uncertainties are shown in Table II.

The actual central value of the beam energy and its spread were measured by looking at the central value and width of the elastic peak in electron proton scattering, as discussed in Section 3.A. Other beam parameters are also shown in Table I.

## B. Targets

The target assembly consisted of 30-cm-long liquid hydrogen and deuterium cells and an empty aluminum dummy cell inside an evacuated scattering chamber.

Any one of the cells could be remotely positioned into the beam path. Table III gives the characteristics of each of the cells. The cells were offset from the center of the beam line by 1.9 cm in the direction of the spectrometer, so that the combined path length of incoming and scattered electron was almost constant, and the scattered particle always went through the endcap. This simplified the radiative corrections calculations. To ensure uniform density inside the cells, the liquid was circulated rapidly by a mechanical pump through the cells and through a liquid-hydrogen cooled heat exchanger. The cells were pressurized to 2 atm to keep them well below the boiling point. To prevent local density changes along the beam line, the liquid in the beam path was mixed with the liquid in the rest of the target by having the fluid enter the bottom of the cells about two-thirds of the way downstream as a jet at an angle of  $45^\circ$  to the beam direction, and exit at the upstream end. During the data taking, the repetition rate of our beam was varied by a factor of two, so we were able to look for possible local density variations of the target with different heat loads. There was no evidence for a density change up to the highest beam currents used in the experiment within the experimental error of about 1%. This uncertainty partially cancels in the ratio of  $\sigma_n/\sigma_p$ , since the beam conditions were similar while collecting data using the hydrogen and deuterium targets (see Table II). The density of the liquids was calculated [24] from measured cell pressure and cell temperature, derived from hydrogen vapor pressure bulbs at both the inlet and the outlet of each cell. The difference between these bulb readings was typically 0.25% and never exceeded 0.5%. This caused a typical uncertainty of about 0.4% in target density. The dummy target cell was a replica of the deuterium and hydrogen cells, except that the aluminum endcaps were 15 times thicker; thus the dummy target was the same radiation length as the deuterium target. This simulated the multiple scattering in the full target, made the radiative corrections similar, and speeded up the data taking.

## C. Spectrometer

The SLAC 20-GeV Spectrometer [20] was used to detect scattered electrons. It is a 50-meter-long system of eleven magnets that transport particles from the target to the momentum and production angle focal planes located in a shielded enclosure, as shown in Fig. 2. The trajectories of particles measured in wire chambers and the magnetic properties of the spectrometer were used to reconstruct the particle's momentum and direction leaving the target. The particle was described in terms of  $\delta p/p$ , the deviation in percent from the central spectrometer momentum  $p_0$ ;  $\delta\theta$ , the deviation in mr from the central spectrometer horizontal angle  $\theta_0 = 10^\circ$ ; the vertical angle  $\phi$ ; and the interaction position along the target length  $z$  as measured from the target center.

The absolute settings of the central momentum of the spectrometer are known to better than  $\pm 0.1\%$  from nuclear magnetic resonance measurements of the bending magnets. The angle [22] of  $10.00^\circ$  has an uncertainty of  $\pm 0.010^\circ$  (0.2 mr), dominated by the uncertainty of the offset of the spectrometer optic axis from the surveyed centerline.

### 1. Detectors

The scattered electrons were measured and identified by a nitrogen gas threshold Čerenkov counter, two planes of plastic scintillation counters, five planes of proportional wire chambers, and a total absorption counter [21,22]. Figure 2 shows the arrangement of the detectors. The first plane of scintillators is 0.318 cm thick to minimize multiple scattering, and is divided into two counters to reduce deadtime. The 2.4-meter-long Čerenkov counter pressure was varied so that pions were always too slow to trigger the counter at each of the spectrometer momentum settings. This produced a clean electron signal, but efficiency for detecting electrons was less than 100% at the highest momentum settings. The Čerenkov

counter was not required for an event trigger. Its efficiency varied between 99.8% at  $p_o = 8$  GeV/c to 97% at  $p_o = 15$  GeV/c.

The total absorption counter was also used to identify electrons and reject pions. It consisted of a 4.3-radiation-length lead-glass Pre-Radiator (PR), followed by a 16-radiation-length lead-lucite sandwich Total Absorption counter (TA). The analogue signals from the PR and TA were linearly added in a proportion that minimized the width of the pulse height spectrum for electrons at the lowest momentum setting (5 GeV/c). The resolution was about  $\pm 13\%$  for momenta between 7 and 14 GeV. This was sufficient for pion rejection, so it was not necessary to optimize the resolution at other energies. Figure 3 shows the spectrum of shower pulse heights for  $Q^2 = 2.5$  [ $p_o = 8$  GeV/c] and  $Q^2 = 10.0$  (GeV/c)<sup>2</sup> [ $p_o = 15$  GeV/c]. With reasonable cuts around the peaks, there is negligible pion contamination and 99.8% efficiency for electrons.

There were five planes of multiwire proportional chambers (MWPCs), three measuring vertical position and two horizontal position. Each chamber was about 20 cm<sup>2</sup> in aperture, and had a wire spacing of 2 mm. The efficiency for finding a single track was about 89%. Most of the inefficiency was due to multiple track ambiguities caused by singles rates. There was a slight rate dependence of about  $\pm 2\%$  to the efficiency over our entire kinematic range. Hydrogen and deuterium target data had equal wire chamber efficiency to within about 1%. We assign an uncertainty of  $\pm 1\%$  for absolute wire chamber efficiency, and  $\pm 0.5\%$  for the uncertainty in the ratio of deuterium-to-hydrogen cross sections.

## 2. *Kinematic reconstruction*

The deviations of the scattering angle and momentum  $\delta p/p$  from the central spectrometer setting were determined from the tracks measured by MWPCs using the magnetic transport coefficients [25]. These were determined from fitting to

particle trajectories measured in 1968. An uncertainty of  $\pm 1\%$  is estimated on the first-order coefficients. A completely independent determination [22] of these coefficients, using scattered electrons and masks to determine angles, had an estimated uncertainty of about  $\pm 2\%$  in first-order coefficients. The results differed by up to 3% in the momentum dispersion term, and 1% in the angle dispersion term. This corresponds to approximately 0.05% in absolute momentum and 0.05 mr at the limits of the acceptance. The 1968 measurements were used for this experiment, since they gave a more physically reasonable acceptance function.

### 3. Acceptance

The nominal acceptance of the spectrometer is  $\delta p/p = \pm 2\%$ ,  $\delta\theta = \pm 4.5$  mr,  $\phi = \pm 8$  mr, and  $x = \pm 3$  cm. The actual acceptance in  $p$ ,  $\theta$ , and  $\phi$  space averaged over our 30-cm-long target seen at  $10^\circ$  is a complicated function determined by many elements in the system. These include various magnet and vacuum chamber apertures, the magnetic transport properties, and the detector sizes. Near the center of the spectrometer ( $\delta\theta = 0$  and  $\delta p/p = 0$ ), the acceptance in  $\phi$  is determined solely by vertical slits at the spectrometer entrance set at  $\pm 8$  mr. No other apertures limit the acceptance in this central region. Thus the acceptance of a bin of nominal size  $\Delta\theta$  by  $\Delta p/p$  in the central region is determined by the product of the first-order magnet coefficients. We assign an overall uncertainty of  $\pm 3\%$  to the acceptance, based on the uncertainty in the coefficients.

We made an accurate experimental determination of the acceptance of the system away from the central area by measuring the response of the spectrometer to an almost uniform flux of electrons, and normalizing it to the central region. We chose a kinematic region where the inelastic structure function  $W_2$  is nearly independent of both  $p$  and  $\theta$  over the acceptance of the spectrometer. The uniform flux is obtained by adjusting the measured cross section by the Nonstructure

cross section. Near the kinematic point  $E = 19.6$  GeV,  $E' = 7.0$  GeV, and  $\Theta = 10^\circ$  ( $x = .18$ ) the structure function  $W_2$  extracted from the cross section, assuming  $R = 0.2$ , has less than a 1% momentum dependence and an angular dependence [26] of approximately  $(1 - .0045 \delta\theta)$  over the spectrometer acceptance.

About 500,000 scattered electrons were detected at these kinematics for our acceptance studies. To measure the momentum dependence of  $W_2$ , and to look at the same scattering kinematics in different parts of the spectrometer, we included spectrometer settings at  $\pm 1.5\%$  from the central setting. The data was accumulated in 36 bins in  $\delta\theta$  in the range  $-5.0 \leq \delta\theta \leq 4.0$  mr and 30 bins in  $\delta p/p$  in the range  $-2.275\% \leq \delta p/p \leq 2.225\%$ . Since the cross section does not depend on the azimuthal angle, and because the vertical angle  $\phi$  is very small compared to the horizontal angle, the data were summed over all values of  $\phi$  at fixed  $\delta\theta$ . The average polar angle of each bin is approximately  $\sqrt{\Theta^2 + \langle\phi^2\rangle}$ , which is within 0.04 mr of  $\Theta$ . The relative acceptance in each bin is then

$$A\left(\frac{\delta p}{p}, \delta\theta\right) = \frac{N\left(\frac{\delta p}{p}, \delta\theta\right)}{\sigma_{NS} [1 + 1.67 (1 + \nu^2/Q^2) \tan^2(\Theta/2)] (1 + .0045\delta\theta)}$$

where  $N$  is the number of counts in each bin, and the denominator is proportional to the cross section calculated above. The absolute acceptance was obtained by normalizing  $A(\delta p/p, \delta\theta) = 16$  mr near  $\delta p/p \sim \delta\theta \sim 0$ .

$A(\delta p/p, \delta\theta)$  is relatively flat in the main region  $-1.975\% \leq \delta p/p \leq 1.925\%$  and  $-5 \text{ mr} \leq \delta\theta \leq 4 \text{ mr}$ . Outside this region, the acceptance has a very sharp dependence on  $\delta p/p$  and  $\delta\theta$ , and was used only for calibration checks—not for the final data analysis. The array  $A$  was fitted to a 40-term polynomial acceptance function in  $\delta p/p$  and  $\delta\theta$  in the main region. The acceptance as a function of  $\delta p/p$  is shown in Fig. 4 for various values of  $\delta\theta$ . Notice the smooth, almost flat acceptance in the main region. Figure 5 shows the acceptance as a function of  $\delta\theta$  for various values

of  $\delta p/p$ . The acceptance is characterized by a double hump that is not produced by any physical obstruction in the spectrometer. This feature is due to errors in the second- and third-order magnetic transport coefficients [25] used to correlate position and angle in the detectors with momentum and angle at the target. An error in the higher order coefficients that produces an error of 0.1 mr in  $\delta\theta$  or 0.1% in  $\delta p/p$  will distort the acceptance by up to 10%. These errors do not effect the acceptance in the region of the spectrometer where the acceptance was normalized. These apparently large distortions of the acceptance function cancel out in the cross section measurement, because in both ‘data’ and ‘acceptance’ measurements the electron spectrum is distorted in an identical manner. In the ratio of deuteron-to-proton cross sections, the acceptance uncertainty mostly cancels, except for an estimated  $\pm 1\%$  due to differences in the shape of the spectra.

The acceptance calculations were checked by studying elastic  $e$ - $p$  scattering and using overlapped spectrum, as discussed below.

#### 4. Resolution

The resolution of the spectrometer is a consequence of multiple scattering, uncertainties in the transport coefficients, the resolution of the wire chambers, the stability of the magnetic fields, the finite target length, and the beam size and emittance. These resulted in a typical momentum resolution of approximately  $\pm 0.08\%$ . The angular resolution was dominated by multiple scattering in the target, and was approximately  $(3.1/p_0)$  mr [22] where  $p_0$  is in GeV/c. This is of the same size as effects causing the distortion in the acceptance mentioned above.

### 3. ANALYSIS AND RESULTS

The main goal of this experiment was to measure the elastic electron-neutron cross section. To do this it was necessary to measure: (1) quasi-elastic electron-deuteron scattering, (2) elastic and inelastic electron-proton scattering in the same

kinematic region, and (3) electron-aluminum scattering from the dummy target. Subsidiary measurements were made in the kinematic region of elastic electron-deuteron scattering (threshold region) from both deuterium and aluminum targets. The elastic electron-proton scattering data were primarily used to extract the  $e$ - $n$  cross section from the  $e$ - $d$  data. They were also used to calibrate the experimental apparatus, as described below. The data from the dummy target was primarily used to subtract the effects of the endcaps of the liquid targets. However, these cross sections have recently become important in their own right. The threshold data is an extension to higher  $Q^2$  of a previous study [27] of scaling in the large  $x > 1$  region.

### A. Calibration from Elastic Peak

The elastic  $e$ - $p$  scattering results were used to measure the performance of our detector. The experimental value of  $W^2$  for the center of the elastic peak is affected by a combination of uncertainties in the beam energy, spectrometer central momentum and angle, and the energy loss in the target. The width of the elastic peak is determined by the energy spread of the incoming beam, momentum and angle resolution of the spectrometer, and radiative effects. The magnitude of the measured elastic cross sections depended on the spectrometer acceptance, beam monitoring, and radiative corrections. A Monte Carlo model of the beam and detector system was created using calculated values of detector resolutions, beam energy spread, and energy loss in the target by both ionization (about 6 MeV for both the incoming and outgoing electrons) and radiation. The beam energy spread was by far the largest contributor to the resolution. The spread had an upper limit determined by the slits (see Table I), and was empirically adjusted in the Monte Carlo until the model matched the experimental spectra, as shown in Fig. 6. The best fit was a Gaussian with  $\sigma = 0.2\%$ , truncated at  $\pm 0.2\%$  by the slits. The central value of the

beam energy relative to the spectrometer momentum setting was determined by comparing the measured and Monte Carlo model position of the elastic peak. The energy of the beam incident on the target, shown in Table I, was determined by assuming that the central spectrometer momentum and angle were exactly known. The difference between nominal and measured beam energy was always  $< 0.15\%$ . The  $Q_{\text{elastic}}^2$  in the table is calculated at the center of the target, including energy loss. Also shown in Table I is the total resolution of the system in missing mass.

Our measurements of the elastic cross section were compared with existing world data to check systematic errors in acceptance and beam monitoring. The elastic cross section data was analyzed in the following manner. Since the elastic cross section changes rapidly with angle (approximately as  $\Theta^{-12}$ ), the experimental cross sections were determined in each of the theta bins within the spectrometer acceptance. These values were then averaged using a fit to previous data [2] to compensate for the angular dependence

$$\frac{d\sigma_p^{\text{el}}}{d\Omega}(10^\circ) = \frac{d\sigma^{\text{fit}}}{d\Omega}(10^\circ) \times \sum_{\Theta} \frac{d\sigma^{\text{exp}}/d\Omega(\Theta)/\delta^2}{d\sigma^{\text{fit}}/d\Omega(\Theta)} \bigg/ \sum_{\Theta} \delta^{-2}$$

where  $\delta$  is the error for each  $\theta$  bin. The answers are independent of the fit used due to the small angular acceptance of the spectrometer. The results were radiatively corrected using the method of Tsai [28]. The cross section was reduced by 2% to 3% due to the inclusion of heavy lepton and quark loops and of energy loss before the scattering [23]. The results for the elastic cross section are shown in Table IV along with the value of a previous fit to world data. Also shown are  $Q^4 G_M^P$  extracted from the cross section assuming form factor scaling ( $G_M^P = \mu G_E^P$ ). This is compared with the same quantity extracted from a recent SLAC experiment [29] using the 8 GeV/c spectrometer at a larger angle and the same beam monitoring equipment. The results agree within the 1% to 2% statistical errors on both experiments.

A recent study [30] of the relative normalizations of the 8 and 20 GeV spectrometers using inelastic scattering measurements showed agreement to the level of 1 to 3%. The acceptance of the 8 GeV/c spectrometer has recently been remeasured [31] to an accuracy of better than 1.5% using a floating wire technique. This cross calibration gives an uncertainty in the absolute acceptance of about  $\pm 3\%$  to the 20 GeV/c spectrometer.

The elastic cross section was measured at each value of  $Q^2$  with central momentum settings of the spectrometer offset by  $-2\%$ ,  $-1\%$ ,  $0\%$ ,  $1\%$ , and  $2\%$  from the nominal setting. This checks the spectrometer acceptance across most of its active region. The measured cross sections at different offsets and  $Q^2$  are consistent with the measurement at zero offset to within the statistical errors, which were about 2% for offsets of  $\pm 1\%$  and about 6% for offsets of  $\pm 2\%$ . There are no systematic differences as a function of spectrometer setting. Table V shows that this agreement averaged over all values of  $Q^2$  is well within the 1 to 3% statistical errors. The optics coefficients of the spectrometer, both in absolute magnitude and as a function of central momentum, were tested by comparing the position of the elastic peak for various spectrometer offsets and different values of  $Q^2$ . The difference of  $W_{\text{elastic}}^2$  for the measured elastic peaks compared to the Monte Carlo model varied at different spectrometer offsets by less than  $\sim 0.005$  (GeV<sup>2</sup>). As a function of central momentum, this difference was independent of spectrometer setting to within the same accuracy. This corresponds to spectrometer momentum uncertainties within the acceptance of  $\delta p/p \leq \pm 0.05\%$ . This limits uncertainties in the first order optics coefficients to  $\leq \pm 3\%$ .

We conclude that the spectrometer acceptance is understood to an accuracy that at least matches the statistical precision of our data.

## B. Quasi-Elastic Spectra

### 1. Analysis

At each incident beam energy, data were collected in a range of spectrometer momentum settings near the quasi-elastic peak. The range extended between  $\delta E'/E'_{\text{elastic}} \sim -4\%$  into the resonance region, and 2% into the region kinematically “forbidden” for  $e-p$  scattering. Data at each spectrometer setting were corrected for electronic dead time (less than 2%) and wire chamber inefficiency (about 12%). Corrections due to shower- and scintillation-counter inefficiencies and pion contamination were negligible. Corrections (typically 3%) for the scattering from target endcaps were made using the dummy target data.

Cross sections were calculated at each momentum and angle bin within the spectrometer acceptance. These were reduced to cross sections at each momentum bin, but at the central spectrometer angle. Because the cross section changes rapidly with  $\Theta$  (for pure elastic scattering,  $\Theta^{-12}$ , but much more slowly for the  $\Delta$  resonance), the contraction over the very small  $\Theta$  acceptance had to be done carefully. Two methods were used. In the first, the  $\Theta$  dependence of the cross section was ignored. We made a weighted average over all  $\theta$  bins, taking into account the spectrometer asymmetric acceptance in  $\theta$ . In the second, we used the maximum  $\Theta$  dependence by making a fit to the  $\Theta$  dependence using the angular functional form of the elastic cross section. The two methods differed by less than 0.5%. The second method was used for final results.

Data from the different spectrometer settings were combined into single spectra for hydrogen and deuterium at each beam energy. Since the spectrometer momentum acceptance was about  $\pm 2.0\%$  and the data were taken with 1% steps of the spectrometer momentum, almost every value of the momentum was covered by three settings of the spectrometer. The data from different spectrometer

settings in the overlapped regions were consistent with each other within the statistical errors. A typical  $\chi^2/\text{degree of freedom}$  of 0.9 was calculated between the overlapped regions of runs with different central momentum. This indicated no significant systematic errors in the acceptance or beam monitoring.

Each spectrum was radiatively corrected using an iterative method based on the peaking approximation of Tsai [28] as implemented by Stein [21]. The peaking approximation is accurate in our kinematic domain, where the energy loss of the electron is small compared to its initial value. The effects of  $\mu$ ,  $\tau$ , and quark vacuum loops, high-order terms in  $\alpha$ , and radiation from the quarks was added according to the prescription of Bardin [32]. These terms decreased the cross sections in our kinematic region by approximately 2% [33]. The peaking approximation radiative correction formalism determines the experimental cross section at a kinematical point from the Born cross section at allowed kinematics of lower incident energy or higher scattered electron energy. Each of our spectrum covered a very limited kinematic region very close to the edges of the effective allowed kinematic limit (elastic scattering for the proton and relatively small cross sections above the quasi-elastic peak for the deuteron). Test models of the Born cross sections based on the experimental data were radiatively corrected, compared with the experimental data, and modified to improve the agreement. This iterative procedure converged rapidly, and was independent of the initial model cross sections. The error due to iteration was  $\leq 1\%$ . The error due to the peaking approximation of Tsai is believed to be about  $\pm 1\%$  in this kinematical region. We assign a total uncertainty of  $\pm 2.0\%$  due to radiative corrections. Most of these uncertainties cancel in the ratio of deuterium-to-hydrogen cross section.

The typical loss due to ionization of both the incoming and outgoing electron was approximately 6 MeV for hydrogen and deuterium targets and 2 MeV for the

dummy target cell. This energy loss is especially significant in kinematic regions where the cross section changes rapidly with these variables. Cross sections for deuterium and hydrogen are reported at the average incident and final energy where the interaction took place in the center of the target. For the comparison of aluminum and deuterium cross sections, where the energy loss was different, both data sets were projected to identical kinematics using appropriate models.

## 2. Results of $e$ - $p$ and $e$ - $d$ quasi-elastic scattering.

The double differential cross section for electron-proton (at five energies) and electron-deuteron (at six energies) scattering are listed in Table VI. The errors are statistical only. The systematic errors are shown in Table II. Figures 7(a) and 7(b) show the proton and deuterium spectra, respectively. Aluminum spectra are discussed in Section 3.D. The inelastic proton cross sections begin at pion production threshold. At low  $Q^2$  there is a clear  $\Delta$  resonance, as well as a peak in the second resonance region. At high  $Q^2$  the  $\Delta$  has subsided into the background, but the second resonance region still has significant signal above background. For the deuteron, the quasi-elastic cross section dominates the spectrum at  $W^2 = 0.88$  for the low  $Q^2$  data, but is less visible at the highest beam energies. The  $\Delta$  resonance is all but invisible due to the smearing caused by the fermi motion of the nucleons.

Figures 8(a) and (b) show the deuterium structure function  $\nu W_2^d$  derived from Eq. (3) under the assumption that the second term is insignificant at  $10^\circ$ . In Fig. 8(a) the deuterium structure function is plotted versus the light cone scaling variable  $\xi = 2x/(1+k)$ , where  $k = \sqrt{1 + (4x^2 M^2/Q^2)}$ . In Fig. 8(b) the deuterium structure function is plotted versus the scaling variable  $\omega' = 1/x + M_p^2/Q^2$ . Also shown in both figures are the threshold measurements of  $\nu W_2^d$  (see Section 3.E), results from SLAC experiment

E101 [34] at  $8^\circ$ , and the fits [30] to SLAC deep inelastic data at  $Q^2 = 5 \text{ (GeV/c)}^2$  (solid) and  $Q^2 = 25 \text{ (GeV/c)}^2$  (dashed). For  $Q^2 \geq 2.5$  and  $W^2 \lesssim M_\Delta^2$ , both  $\nu W_2^d(\xi, Q^2)$  and  $\nu W_2^d(\omega', Q^2)$  are approximately independent of  $Q^2$ , except for quasi-elastic peaks. These peaks decrease rapidly with  $Q^2$ , and are almost indistinguishable by  $Q^2 = 10 \text{ (GeV/c)}^2$ . By contrast, the deep inelastic data has a large-scale breaking in this high  $x$  region. Thus scaling derived from the quark-parton model is approximately valid, even for the kinematic region of the resonance region and the quasi-elastic scattering tails.

### C. Elastic Neutron Cross Section

The neutron elastic cross section was extracted from the deuteron and proton spectra by modeling the effects of the neutron being bound inside of the deuteron. We assumed that the electron scattering in the deuteron was correctly represented by a spectator model in which only one nucleon was struck by the virtual photon and the other was unaffected by the interaction. The Fermi motion of the struck nucleons was obtained from phenomenological deuteron wave functions. In addition, the deuteron cross section was assumed to be separable into an incoherent sum of elastic and inelastic scattering from the nucleons inside the deuteron. We thus used a model of the deuteron cross section consisting of four parts: (1) quasi-elastic  $e$ - $p$  scattering; (2) quasi-inelastic  $e$ - $p$  scattering; (3) quasi-elastic  $e$ - $n$  scattering; and (4) quasi-inelastic  $e$ - $n$  scattering. The first two parts, the smeared proton cross sections, were generated using the corresponding measured electron proton cross sections and the effects of binding in the deuteron. The last two parts, the smeared neutron cross sections, were assumed to be proportional to the corresponding smeared proton cross sections. The two proportionality parameters,  $\sigma_n^{\text{el}}/\sigma_p^{\text{el}}$  and  $\sigma_n^{\text{in}}/\sigma_p^{\text{in}}$ , were determined by comparing the model deuteron cross

sections with the experimental deuteron cross sections over a large range of missing mass squared, from the quasi-elastic region to the first resonance region. The inelastic neutron contribution was determined primarily by the data in the resonance region where the quasi-elastic contributions are small.

Two different approaches were used to simulate the deuteron binding. Both used models of the deuteron wave function to describe the motion of the nucleons. A variety of wave functions were used to determine the sensitivity of our results to this theoretical input.

### **1. Monte Carlo method**

The first method used a Monte Carlo model of the entire experimental apparatus, including resolution, radiative losses, beam energy, etc., to generate the elastic ( $\sigma^{qel}$  model) and inelastic ( $\sigma^{qin}$  model) parts of the smeared proton contribution to the experimental deuteron spectrum. The scattering on bound nucleons was simulated event-by-event. The deuteron wave function determined the momentum of the struck nucleon. The spectator nucleon was assumed to be on mass shell and did not have any final or initial state interactions with the struck nucleon. The struck nucleon was off mass shell, but no correction to the scattering for off-shell form factors was made. A flux factor accounted for the motion of the target nucleon. The initial conditions of the struck nucleon (Fermi momentum and angle) were uniformly generated in the lab rest frame. Electron scattering took place in the rest frame of the struck nucleon. The electrons were uniformly distributed in scattering angle and generated missing mass ( $W_{gen}^2$ ) and weighted by the cross section at those kinematics and the probability distribution of the Fermi momentum. Events were generated at all kinematics that would result in scattered electrons entering the spectrometer acceptance. We used our elastic and inelastic proton

cross section as input to cancel any effects due to overall systematic uncertainties in the apparatus. However, because of the Fermi motion of the nucleon, the generated scattering kinematics covered a range in incident energy, and scattered energy and angle not measured using our proton target. We extended our range by using a parameterization of previous SLAC data in the resonance region [26] to interpolate between our measured spectrum in energy, and to extend the angular and missing mass range. The parameterization was normalized to our data to minimize any systematic errors.

Most of the quasi-elastic peak is in the laboratory frame kinematic region  $0.7 \leq W^2 \leq 1.1 \text{ GeV}^2$ . Detected electrons with missing mass in this region can actually have scattered inelastically at quite different kinematics in the struck nucleon rest frame, due to the Fermi motion. Using the Monte Carlo Model, we have determined the kinematics in the nucleon rest frame for quasi-inelastically scattered electrons that are within this laboratory  $W^2$  range and are within the spectrometer acceptance. In Figs. 9 and 10 the Holinde-Machleidt [35] model 3 of the deuteron wave function was used. Figure 9 shows the percentage of events/ $\text{GeV}^2$  in the quasi-elastic region, as a function of  $W_{\text{gen}}^2$  in the nucleon rest frame at high and low  $Q^2$ . This is a convolution of the inelastic cross section that increases rapidly with  $W_{\text{gen}}^2$ , the Fermi momentum and the spectrometer acceptance. At the larger value of  $Q^2$ , the electron scattering in the nucleon rest frame typically occurs at much larger values of generated missing mass. Figure 10 shows the percentage of events/MeV as a function of generated Fermi momenta for two values of  $Q^2$ . In both cases, the events that are in the quasi-elastic kinematic region are centered at a Fermi motion far larger than the unbiased Fermi momentum distribution (dotted line), which is centered at  $\sim 50 \text{ MeV}/c$ . Thus our models of the cross section in this kinematic region are very sensitive to the high momentum components of the deuteron. At high  $Q^2$  there is a large contribution of events with

very large Fermi motion that contribute to the low missing-mass end of the quasi-elastic region in addition to the events with Fermi momentum of  $\sim 150$  MeV/c which contribute to the high missing mass end. Thus as  $Q^2$  increases, there is a correspondingly larger kinematic range in the nucleon rest frame and a greater contribution from the high-momentum components of the deuteron wave function.

At each incident beam energy, a linear least-square fit to the form

$$\sigma_d^{\text{exp}} = (1 + \sigma_n^{\text{el}}/\sigma_p^{\text{el}})\sigma_p^{\text{qel model}} + (1 + \sigma_n^{\text{in}}/\sigma_p^{\text{in}})\sigma_p^{\text{qin model}} \quad (5)$$

determined the best values of  $\sigma_n^{\text{el}}/\sigma_p^{\text{el}}$  and  $\sigma_n^{\text{in}}/\sigma_p^{\text{in}}$  to match the model and experimental deuteron cross sections over a large range of  $W^2$ .

The accuracy of our model of the tail of the quasi-inelastic spectrum underneath the quasi-elastic peak was the limiting uncertainty at high  $Q^2$ . At  $Q^2 = 10$  (GeV/c)<sup>2</sup>, the Monte Carlo models were unable to reproduce the experimental spectrum with consistent values of the fitting parameters. The results depended on the range of  $W^2$  that was used for the fit. This was due in part to the increasing range of center of mass kinematics caused by the Fermi motion, as shown in Figs. 9 and 10. Extensions of the model would have required large investments in computer time and thus, for  $Q^2 = 10$  (GeV/c)<sup>2</sup> it was abandoned in favor of the  $y$ -scaling method described below.

Figure 11 shows the experimental deuterium cross sections before radiative and energy loss corrections were applied, and typical fits to the sum of Monte Carlo generated quasi-elastic and quasi-inelastic contributions from the proton and neutron. The kinematic range of the fits is  $0.3 \leq W^2 \leq 1.9$  (GeV/c)<sup>2</sup> for  $Q^2 \leq 8$  (GeV/c)<sup>2</sup>. The Reid Soft Core potential was used [36] for the deuteron wave function. Figure 12 shows the difference between the measured deuteron spectra and the same model. While the cross sections vary by well over an order

of magnitude, the model reproduces the experimental cross section over the entire range of  $W^2$  to within a few percent. There is a slight deviation at and below the quasi-elastic peak at low  $Q^2$ , where the model is slightly narrower than the measured cross section and another deviation just below the  $\Delta$ . Several different representative models of the deuteron wave function were used in the analysis. They included the Reid Soft Core and the Holinde-Machleidt [35] models 2 and 3. Variations on each of these were created using the  $(e, e'p)$  measurements at Saclay [37] to enhance the high momentum components of the wave function. The probability of the nucleon having a Fermi momentum,  $p_f > 300$  MeV/c was varied between 2% and 4%. The Paris Potential [38], while not used explicitly, fell within the range of models used. Models with  $> 6\%$  probability for  $p_f > 300$  MeV/c, (such as the Lomon-Feshbach [39] with 7.5% d-state) were unable to fit the deuteron spectrum, and were not included. Table VII shows the extracted value of  $\sigma_n^{\text{el}}/\sigma_p^{\text{el}}$  using several different values of the deuteron wave function. Also shown is the  $\chi^2/\text{df}$  for the fit done in the range  $0.4 \leq W^2 \leq 1.5$  (GeV/c) $^2$ . The results are insensitive to the  $W^2$  range used. The ratio  $\sigma_n^{\text{in}}/\sigma_p^{\text{in}}$  from the fits, with total error is  $0.58 \pm 0.02$ ,  $0.47 \pm 0.02$ ,  $0.49 \pm 0.03$ , and  $0.33 \pm 0.06$  at incident energy = 9.744, 12.589, 15.726 and 18.476 GeV. These ratios are averaged over the range  $W^2 \lesssim 2$  GeV $^2$ . The errors are smaller than in the elastic case, because of less sensitivity to beam parameters and spectrometer acceptance, as well as deuteron models.

## 2. *y-Scaling Method*

The second method for simulating the deuteron binding used analytic formulas to generate the shapes of the elastic and inelastic contributions. These were then fitted to the radiatively corrected spectra using a single normalization factor for each of the two contributions. This method had the advantage that it took much

less computer time, so that many different wave function models could be tried. The elastic contributions were generated using a simplified version of the Plane-Wave Impulse Approximation (PWIA) of McGee [40] given by

$$\frac{d\sigma}{d\Omega dE'} = \sigma_p^{\text{el}} \frac{M_p^2}{2q} \frac{E}{E'} \int_{|y|}^{|y+q|} \frac{[u^2(k) + v^2(k)]k dk}{\sqrt{k^2 + M_p^2}}$$

where  $q$  is the absolute value of the three-momentum transfer,  $u$  and  $v$  are the s-wave and d-wave deuteron wave function components, and  $|y|$  is the minimum fermi momentum for the spectator nucleon, assuming it is on mass-shell. It's value can be found from the solution of

$$E + M_d = E' + \sqrt{M_p^2 + (q + y)^2} + \sqrt{(M_d - M_p)^2 + y^2}$$

where  $M_d$  is the mass of the deuteron. The variable  $y$  has a particular significance since scaling functions such as

$$F(y) = \frac{d\sigma}{d\Omega dE'} \frac{dE'}{dy} \frac{1}{(Z\sigma_p + N\sigma_n)}$$

have been shown [41] to be independent of  $Q^2$  and  $E$  at fixed  $y$  to a perhaps surprising degree of accuracy. We have compared our simplified model for the cross section to the full McGee calculation, using a fixed deuteron wave function, and find that for the kinematic range of this experiment, the differences are much smaller than those arising from using different choices for the deuteron wave function.

The observation that this very simple function can reasonably describe the shape and magnitude of the quasi-elastic peak was used to invent an analytic

method to apply Fermi-smearing to the inelastic proton data. The equation used was

$$\frac{d\sigma_p^{\text{qin}}}{d\Omega dE'} = \int \frac{d\sigma_p^{\text{in}}}{d\Omega dE'} R(y) G(y) dE'$$

where  $\int G(y) dE' = 1$  and  $G(y)$  is given by

$$G(y) = \frac{M_p^2}{2q} \frac{E}{E'} \int_{|y|}^{|y+q|} \frac{(u^2(k) + v^2(k)) k dk}{\sqrt{k^2 + M_p^2}}$$

The definition of  $y$  was modified to take into account the larger invariant mass of the final state. The factor  $R(y)$  is 1 for  $y = 0$  and accounted for the  $Q^2$  dependence of the inelastic proton cross-sections. Both the fermi-smearred elastic and inelastic cross sections were convoluted with the experimental resolutions before being fit to the data.

Values for  $\sigma_n/\sigma_p$  were extracted from the two-parameter fits to the data in a manner similar to that of the Monte Carlo method. The results, along with the  $\chi^2/\text{d.f.}$  for the fits, are shown in the first four entries in Table VIII for four different model wave functions:

- the Lomon-Feshbach with 7.2% d-state [39],
- the Reid soft-core [36],
- the Paris [38], and
- the 1987 version of the Bonn potential [42].

It can be seen that the  $\chi^2$  values for  $Q^2 \leq 6$  (GeV/c)<sup>2</sup> are not very good for any of the potentials, but are reasonable for the two highest  $Q^2$  points for all except the Bonn potential (this is the one with the smallest amount of high momentum components). The reason the fits are not good for the lower  $Q^2$  data can be seen

in Fig. 13, which shows the ratios of the data to the fits using the Paris wave function. The ratios are less than one at the quasi-elastic peak ( $W^2 = 0.88$ , or  $y = 0$ ), and rise above one for lower values of  $W^2$ . The same trend was seen for the other three potentials used, and corresponds to the model for the quasi-elastic peak being too narrow (not enough high-momentum components).

To obtain better fits to the data, a multiplicative correction factor  $C(y) = 1 + c_1|y| + c_2y^2$  was applied to  $F(y)$  for both the elastic and inelastic models. To find the coefficients  $c_1$  and  $c_2$ , data from this and from several other experiments [43] were examined. The ratios of the data to the McGee model using the Paris potential were determined as a function of  $Q^2$  for several different  $y$  bins, as illustrated in Fig. 14. The trend of the ratios is to decrease with  $Q^2$ , and then roughly flatten out to an asymptotic value. This trend can also be seen in the full calculations of Laget [44] and Arenhövel [45], which both include final-state interactions and meson-exchange currents. We have made a fit to the asymptotic values for each  $y$  bin to determine the correction coefficients  $c_1$  and  $c_2$ . Given the uncertainties in the asymptotic limits, we found four choices for  $c_1$  and  $c_2$  that gave equally good fits. The results for  $\sigma_n/\sigma_p$  using these four choices are shown as the fifth through eighth entries in Table VIII. It can be seen that a considerable improvement in the  $\chi^2$  values at low  $Q^2$  is obtained for all four choices. The  $\chi^2$  values for  $Q^2 \leq 6$  (GeV/c)<sup>2</sup> are still significantly above 1.0, however, with most deviations now coming from the region around  $W^2 = 1.5$  GeV<sup>2</sup>, which can be seen in Fig. 15. This corresponds to the peak of the  $\Delta(1236)$  resonance, and could be caused by a nonconstant ratio for  $\sigma_n/\sigma_p$  in the inelastic region. For lack of a good model on how to solve this problem, we have not tried to use  $\sigma_n/\sigma_p$  ratios that vary in the inelastic region.

Now that we had models that gave good  $\chi^2$  values in the quasi-elastic region ( $W^2 < 1.3$  GeV<sup>2</sup>), we used one of the choices for  $c_1$  and  $c_2$  and tried the different wave functions. The results are shown as the last three entries in Table VIII.

It can be seen that the choice of wave function has little effect at low  $Q^2$ , but changes the results for  $\sigma_n/\sigma_p$  dramatically at high  $Q^2$ , where the relative importance of the inelastic contributions are much larger. The relative importance of the elastic and inelastic contributions is illustrated in Fig. 16. The inelastic contributions are sensitive, on the average, to larger Fermi-momentum values, and so depend much more on the choice of potential than the quasi-elastic contributions do.

Given the uncertainties in the models, it is hard to determine an error bar for the elastic  $\sigma_n^{\text{el}}/\sigma_p^{\text{el}}$  results. Instead, we list in the bottom row of Table VIII the range of answers for which reasonable  $\chi^2$  values were obtained. It can be seen that the range is rather limited at low  $Q^2$ , but increases strongly with  $Q^2$ . The results of the analytic method are similar to those obtained independently with the Monte Carlo method described earlier.

Both methods described above assume that the ratio  $\sigma_n^{\text{inel}}/\sigma_p^{\text{inel}}$  is a constant over our kinematic range, and that there is no EMC effect in the deuteron [18]. Sargsyan et al. [46] have used light-cone quantum mechanics of the deuteron [14], a varying neutron to proton ratio, and various models of the EMC effect to extract the elastic form factors from our deuteron cross sections. Their results for  $\sigma_n^{\text{el}}/\sigma_p^{\text{el}}$  are larger than ours, especially at larger values of  $Q^2$ .

### 3. Results

Table IX gives the ratio of elastic scattering  $(d\sigma_n^{\text{el}}/d\Omega)/(d\sigma_p^{\text{el}}/d\Omega)$  averaged over our two methods. Only the deuteron potential models that gave a reasonable  $\chi^2$  per degree of freedom ( $\leq 1.6$ ) over most of the  $Q^2$  range were used. The error due to the model dependence was estimated as the one standard deviation range among the potentials used. As our knowledge of the high-momentum components of the deuteron wave function increases, and calculations of the inelastic smearing

become more sophisticated, the cross section data in Table VI can be refit to give a smaller model dependence to the results. At high  $Q^2$ , the errors are completely dominated by the systematic uncertainty due to extracting the neutron cross section from the deuteron spectrum. The statistical errors are only a few percent, as are systematic errors due to the beam, target, and detectors discussed above. The ratio is insensitive to systematic uncertainties in the absolute acceptance, beam flux, beam energy and spectrometer settings.

Figure 17 shows our ratio of cross sections compared with results from some of the previous experiments [47], and with selected predictions and fits. Data at large angle has been projected to  $10^\circ$  by assuming form factor scaling. Other experimental data [48] at lower  $Q^2$  are not shown. The new results are in good agreement (but slightly lower) than those from previous experiments that overlap the lower end of our  $Q^2$  range. The cross section ratios decrease with increasing  $Q^2$  above  $Q^2 = 6 \text{ (GeV/c)}^2$ , albeit with large errors. This decrease is insensitive to the choice of deuteron potential model and to the method of extraction of the neutron cross section. As seen in Tables VII and VIII,  $\sigma_n^{\text{el}}/\sigma_p^{\text{el}}$  decreases for all methods and models that have reasonable fits to the data. The results of Sargsian [46] are also consistent with this decrease.

Elastic cross section data is often described [1,49] in terms of form factor scaling ( $G_E^P = G_M^P/\mu_P = G_M^N/\mu_N$ ), which is fairly consistent with both previous data and preliminary NE11 data [50] from SLAC. The common assumption [49] that  $G_E^N \sim 0$  then yields values of  $\sigma_n^{\text{el}}/\sigma_p^{\text{el}}$  which are consistent with the data up to  $Q^2 = 6$ . However, at larger values of  $Q^2$ ,  $\sigma_n^{\text{el}}/\sigma_p^{\text{el}} \rightarrow (\mu_n/\mu_p)^2 \sim 0.47$ , which is higher than our measurements. If we instead assume a completely neutral neutron [8],  $F_{1n} = 0$ , then  $\sigma_n^{\text{el}}/\sigma_p^{\text{el}} \rightarrow (1 + Q^2/4M_p^2)/2$  at large  $Q^2$ . This is also inconsistent with the new data.

At large  $Q^2$ , the Dirac and Pauli Form factors are expected to have a  $Q^2$  dependence determined by the quark counting rules [51]  $F_1 \sim C_1/Q^4$  and  $F_2 \sim C_2/Q^6$ , where the C's are constants. Using Eq. (2),  $\sigma_n^{\text{el}}/\sigma_p^{\text{el}} \sim (C_{1n}^2 Q^{-8} + C_{2n}^2 Q^{-10}) / (C_{1p}^2 Q^{-8} + C_{2p}^2 Q^{-10})$ . Different quark wave functions yield different values of  $C_{1n}/C_{1p}$ . For example, if only the same flavor [8] (spin [52]) quarks occupy the high momentum region for the scattering,  $C_{1n}/C_{1p} = -1/2$  ( $-1/3$ ) and  $\sigma_n^{\text{el}}/\sigma_p^{\text{el}} = .25$  (.11). With the above  $Q^2$  dependence, the assumption [8]  $F_{1n} = 0$  yields  $\sigma_n^{\text{el}}/\sigma_p^{\text{el}} = C_{2n}^2/Q^2$ . All three examples are consistent with the new data.

The concepts of Vector Meson Dominance (VMD) have been used to fit previous data and predict  $\sigma_n^{\text{el}}/\sigma_p^{\text{el}}$ . Extended VMD models [2,3,5,6] include many high-mass vector mesons to get the correct  $Q^2$  dependence of the form factors. The predictions of Blatnik and Zovko [3] fall below the data at low  $Q^2$ , but agree with the data at the two largest values of  $Q^2$ . The model of Hohler [5] shown in Fig. 17 has a very small value of  $G_E^N$ , and the ratio of cross sections increases rapidly with  $Q^2$ , in disagreement with the data. On the other hand, the fit of Korner and Kuroda [6] has a very small value of  $F_{1n}$ , due to cancellation caused by the nearly equal masses of the  $\omega$  and  $\rho$  and the  $\omega'$  and  $\rho'$  respectively. There is a small value of  $G_E^P$  with respect to the dipole and a relatively large value of  $G_E^N$ . The results match the  $Q^2$  dependence of  $\sigma_n^{\text{el}}/\sigma_p^{\text{el}}$ , but are somewhat too large in magnitude.

The hybrid model of Gari and Krumpelmann [10] has the long-range low  $Q^2$  region determined by the low-lying vector mesons, and the high  $Q^2$  region determined by the quark-counting rules. The authors also incorporate an asymmetric quark wave function for the neutron and proton. A cancellation of terms from the quarks leads to a small value of  $F_{1n}$ , and hence to a decreasing value of  $\sigma_n^{\text{el}}/\sigma_p^{\text{el}}$ .

It appears that models in which  $F_{1n}$  is small are able to match the decreasing value of  $\sigma_n^{\text{el}}/\sigma_p^{\text{el}}$  as  $Q^2$  increases. These models have quite different theoretical

underpinning, and very different predictions for the neutron and proton electric form factor.

#### D. Aluminum Cross Sections

We measured the ratio of cross sections from aluminum and deuterium targets over a wide kinematic range. The ratio has smaller systematic errors and has more physics interest than the aluminum cross section alone. Data were collected on electron scattering from the dummy cell at each value of incident energy, for the purpose of subtracting the contributions of the aluminum endcaps on the hydrogen and deuterium target spectra. The characteristics of the dummy cell are given in Table III. These data were also used to determine the electron-aluminum cross section. The ratio of spectrometer acceptance for the dummy cell to the full cells was  $0.97 \pm 0.03$  for the restricted angular range of  $-3.5 \text{ mr} \leq \delta\theta \leq 2 \text{ mr}$ . This was determined by taking the ratio of normalized counting rates for full and dummy cells in a kinematic region ( $x = 0.18$ ,  $Q^2 = 4 \text{ (GeV/c)}^2$ ,  $W^2 = 20.3 \text{ GeV}^2$ ), where there is little structure in the cross sections and there is no difference between the cross section per nucleon from aluminum and deuterium. This is shown in Fig. 18. The ratio is  $\sim 0.6$  at low and high  $\delta\theta$  because only one of the two dummy endcaps is viewed by the spectrometer in that region.

Most of the aluminum data were analysed in the same way as the deuterium and hydrogen data described above. However, for some of the kinematic points at large  $x$ , there were insufficient statistics to fit the  $\delta\theta$  dependence within the spectrometer acceptance. For those points, we took the average cross sections over the spectrometer acceptance for both the aluminum and the deuterium data. Due to the strong  $\theta$  dependence of the cross sections, this averaging method does not give a good estimate of the cross sections at the central angle of the spectrometer. However, the cross sections from both targets have approximately the same  $\delta\theta$

dependence. The ratio of aluminum-to-deuterium cross sections is only sensitive to the difference in  $\delta\theta$  dependence. The effects of this difference on the cross section ratio is consistent with zero, with errors up to 5%. This error is small compared to the statistical error at these large  $x$  kinematics.

The aluminum data were radiatively corrected in the same manner as the deuterium data described above. Because both aluminum and deuterium targets had the same radiation length, the radiative corrections differed by a maximum of 15%. This difference is due to the different shape of the two spectra and the target geometry. The aluminum cross sections were adjusted to the cross sections from a symmetric nucleus of atomic number 27, with equal number of protons and neutrons using:

$$\sigma_{Al} = \left( \frac{2Z}{A} + \frac{2(A-2Z)}{A} \cdot \frac{\sigma_n/\sigma_p}{(1 + \sigma_n/\sigma_p)} \right) \sigma_{Al}^{\text{sym}} .$$

The ratio  $\sigma_n/\sigma_p$  is approximately 0.35 in the quasi-elastic and 0.5 in the resonance region from the fits to the deuterium spectrum described above. This yields an approximately uniform adjustment of 1.5% over the entire kinematic range of this experiment. The different energy losses due to ionization in the two targets was included as part of the radiative correction procedure by using the model cross sections. This resulted in adjustments of up to 15% in the ratio due to the very rapidly changing cross section with scattered electron energy in the kinematic region  $W^2 \ll M_p^2$ .

The ratio of adjusted aluminum to deuterium cross sections is shown in Fig. 19 and in Table 6. For the lowest energies the ratio  $\sigma_{Al}/\sigma_d$  is considerably less than unity near the quasi-elastic peak,  $W^2 = 0.88 \text{ GeV}^2$ , because the Fermi motion in aluminum broadens the peak more than in deuterium. At higher  $Q^2$  the quasi-elastic peak and resonances become less important compared to the inelastic continuum and the ratio shows little or no structure. At  $x > 1$ , the ratio becomes

quite large, reaching approximately  $4.0 \pm 0.5$  at  $x = 1.5$  for  $E=9.761$ . Data at  $Q^2 \sim 7$  (GeV/c)<sup>2</sup>,  $E=17.301$ , and  $x \geq 1.5$  has a ratio of  $\sigma_{Al}/\sigma_d \sim 5 \pm 1.5$ .

Theoretical models predict that this ratio is sensitive to the nucleon correlations within the nucleus. Frankfurt and Strikman [53] give a rough estimate of seven for this ratio in the pair correlation approximation. If three-nucleon correlations are included, the ratio is about 30—well above the data. Vary [54] predicts that the ratio in the region  $1 \leq x \leq 2$  is given by the ratio of probabilities for two-nucleon clusters in the two nuclei, which is about three in his models [55]. It seems that the large values of  $\sigma_{Al}/\sigma_d$  can be explained by short range correlations among the nucleons without resort to more exotic degrees of freedom. Frankfurt and Strikman [14] have also compared these results with a model that calculates both the effects of inelastic scattering [53] and quasi-elastic scattering using a realistic aluminum wave function including the possibility of the swelling of nucleons inside the nucleus. They find good agreement with our data, with no swelling, and conclude that the change in  $G_M$  inside the aluminum nucleus compared to deuterium is less than 5% to 10%.

### E. Threshold Cross Sections

Cross sections were measured from deuterium and aluminum targets at an incident energy of 17.327 GeV near the threshold break-up region for deuterium (near the kinematics for elastic electron-deuteron scattering). This corresponded to  $Q^2 = 8.0$  (GeV/c)<sup>2</sup> at threshold, where the cross sections were extremely small. The data took several days to collect, and only 160 events were recorded from the deuterium target and 18 from the aluminum dummy target. Even at these low electron-counting rates, pions and electrons were unambiguously separated in the shower counter. Elastic electron-proton calibration runs at the same beam energy were interleaved with the electron-deuteron data collection to monitor the

detector and beam performance. The beam energy and other characteristics from these calibrations are shown in Table I.

### 1. *Threshold deuterium data*

The data was analyzed in a variety of ways to determine the stability of the results with respect to binning and other effects. Cross sections obtained by either fitting or averaging over the angular acceptance of the spectrometer, yielded results that agreed to much better than their statistical precision. Within errors, the results were also independent of the way the data were binned in the physics variables  $E'$ ,  $W_d^2 = M_d^2 + 2M_d(E - E') - 4EE'\sin^2(\Theta/2)$  [the missing mass of the entire hadronic system including both nucleons], or  $\omega' = M_p^2/Q^2 + 1/x$ . The radiative corrections were obtained by an iterative method, as described above. Within the statistical uncertainty of the procedure, the corrections were a uniform factor of two. The resolution is approximately  $\pm 0.13$  in  $W_d^2$  and  $\pm 0.06$  in  $W^2$ , which is equivalent to a cross section uncertainty  $\sim \pm 3\%$ .

Figure 20 shows the deuterium cross sections in pb/GeV/sr as a function of  $W_d^2$ , the variable appropriate for showing any structure in the two nucleon system. The inelastic threshold is at  $W_d^2 = 3.52$ . A fit to the cross section increases very roughly as  $3 \times 10^{-6} \exp\{1.92W_d^2\}$  pb/sr-GeV per average nucleon. There is a 2.2 standard deviation enhancement above the fit at  $W_d^2 = 5$ . There is a 25% probability of finding a fluctuation this large in any of our nine data points.

It was predicted in a study of the asymptotic form factors and the connection of nuclear and nucleon dynamics [8], that the inelastic scattering near threshold takes place via the elastic scattering from individual nucleons within the nucleus. These ideas were extended by other authors [56,57] to include scattering from

clusters of nucleons or quarks within the nucleus. For the deuteron, the structure function would factor into

$$\nu W_2(x_d, Q^2) \sim A_N(Q^2) x_d G(x_d), \quad (6)$$

where  $A_N(Q^2)$  is the square of the elastic nucleon form factor, and  $G(x_d)$  is the probability for the nucleon to have fractional momentum  $x_d = Q^2/(2M_d\nu)$  in the infinite momentum frame of the deuteron. The quark spectator counting rules [58] were generalized [8] for nuclei of atomic number  $A$ , with  $A - 1$  spectator nucleons to give  $G(x_d) \sim (1 - x_d)^{6(A-1)-1}$ . For the deuteron, with scattering from single nucleons,  $G(x_d) \sim (1 - x_d)^5$ . If the deuteron as a single entity was struck, then  $G(x_d) \sim (1 - x_d)^{-1}$ . We extracted  $\nu W_2/x_d$  at  $Q^2 = 8$  (GeV/c)<sup>2</sup> from our data assuming the contribution from  $W_1$  is small at  $\Theta = 10^\circ$ , and have plotted the results versus  $(1 - x_d)$  in Fig. 21 along with results at lower  $Q^2$  from previous experiments [34]. At  $Q^2 = 8$ , the function  $\nu W_2/x_d$  is linear on the log-log plot, with a slope of  $3.8 \pm 0.5$ , in rough agreement with the predicted power of 5. At lower values of  $Q^2$ , the power of  $(1 - x_d)$  is smaller than 3 in the region  $0.2 \leq 1 - x_d \leq 0.3$ . Very close to threshold,  $\nu W_2/x_d$  is almost independent of  $1 - x_d$ . The QCD prediction of a power of  $2n_s - 1 = 9$ , where  $n_s$  is the number of quark spectators in the deuteron (5), is inconsistent with the data. Thus at the highest  $Q^2$ , the results are consistent with scattering from single nucleons within the deuteron at high  $Q^2$ , but there may be significant contributions from scattering from the deuteron as a single entity very close to threshold, where the power dependence is slight.

For the low  $Q^2$  kinematic region, it is appropriate to use the light cone scaling variable  $\xi$ . Figure 22 contains  $\nu W_2/\xi$  as a function of  $\xi_{max} - \xi$  for the same data as in Fig. 21. The same power law trends are apparent in both figures. Because most of the data is compressed into a similar range of  $\xi$ , it is sensible to compare the

power law behavior at each  $Q^2$ . In the kinematic range  $0.05 \leq \xi_{max} - \xi \leq 0.17$ ,  $Q^2 \geq 1.5$ , the best fit is  $\nu W_2/\xi \sim 2.4(\xi_{max} - \xi)^n/(Q^2)^{5.8}$  where  $n \sim 1.8 \pm 0.3$ . This is shown in Fig. 22 as a solid line, while the dashed lines show the continuation of the fit to higher and lower values of  $\xi_{max} - \xi$ . For  $Q^2 = 8$  at the larger values of  $\xi_{max} - \xi$ , the power law in  $\xi_{max} - \xi$  is twice as large, while for lower values of  $Q^2$  and smaller values of  $\xi_{max} - \xi$ , the power fall off is much smaller. The power of  $Q^2$  is higher than the value of four expected from scattering from a single nucleon.

## 2. Elastic-inelastic connection

It has been suggested by several authors [59,60] that there is a relationship between elastic electron-nucleus form factors ( $x_d = 1$ ) and inelastic threshold structure functions ( $x_d \sim 1$ ) that depends on which constituents are scattered from inside the nucleus. Brodsky and Chertok [8] derived the relationship using Eq. (6), with the extra powers of  $Q^2$  coming from  $(1 - x_d)^n$  at fixed  $W_d^2$ . They obtained

$$\frac{d\sigma_d}{d\Omega dW_d^2} = \frac{d\sigma_d^{el}}{dQ^2} \rho(W_d^2). \quad (7)$$

If the electron-deuteron elastic cross section is written as

$$\frac{d\sigma_d^{el}}{d\Omega} = \sigma_{\text{Mott}} [A_d(Q^2) + B_d(Q^2) \tan^2(\Theta/2)]$$

then Eq. (7) becomes

$$\frac{W_2^d(Q^2, W_d^2)}{A_d(Q^2)} = C(W_d^2). \quad (8)$$

This relationship was found to be consistent with previous results on elastic [61] and inelastic [34] electron-deuteron scattering. Figure 23 shows  $W_2^d/A_d$  as a function of  $Q^2$  for several values of  $W_d - M_d$  near the elastic threshold, derived from a reanalysis of that data [34].

For  $Q^2 \geq 2.5(\text{GeV}/c)^2$ , the ratio becomes independent of  $Q^2$  as expected from Eq. (8). Table X gives the average values of  $W_2/A$  for  $Q^2 \geq 2.5(\text{GeV}/c)^2$  at several different values of  $W_d - M_d$ . If we *assume* Eq. (8) to be valid, we can determine  $A_d$  at  $Q^2 = 6$  and  $8 (\text{GeV}/c)^2$  from the measured values of  $W_2$  in the previous experiment [34] and this experiment, respectively. The results are shown in Table X. The errors are statistical only, and *do not* include the considerable theoretical uncertainty in Eq. (8). Since these elastic form factor results are *indirect* measurements, they should be used, if at all, with extreme caution.

#### 4. SUMMARY

We have measured electron-deuteron and electron-proton cross sections at  $10^\circ$  from near their respective thresholds into the resonance region. We have also measured the electron-aluminum cross section near the deuterium breakup threshold and near the quasi-elastic peak. The inelastic deuteron spectrum in the region of the quasi-elastic peak is roughly consistent with expectations from scattering from a single nucleon. A variety of models of the deuteron wave functions are capable of reproducing our results. The deuterium cross sections from threshold thru the resonance region are also consistent with models based on single quark knock out and an approach to scaling using either the Nachmann variable  $\xi$  or the Bloom-Gilman variable  $\omega'$ . The ratio of inelastic cross sections per nucleon,  $\sigma_{Al}/\sigma_d$  increases from less than one at  $x = 1$  to approximately four at  $x = 1.5$ .

The elastic electron-neutron cross section was extracted from the quasi-elastic data out to  $Q^2 = 10 (\text{GeV}/c)^2$ . The ratio  $\sigma_n^{\text{el}}/\sigma_p^{\text{el}}$  appears to decrease with increasing  $Q^2$  above  $Q^2 = 6 (\text{GeV}/c)^2$ . This is inconsistent with form factor scaling for  $G_M^P$ ,  $G_E^P$ , and  $G_M^N$  combined with either  $G_E^N = 0$  or  $F_1^N = 0$ . It is consistent with the form factors falling with powers of  $Q^2$ , determined by dimensional scaling laws combined with a variety of nucleon wave functions. It is also consistent with some

models based on Vector Dominance and a combination of Vector Dominance, and QCD. Future measurements of  $G_E^P$  and  $G_E^N$  are necessary to distinguish between these approaches.

## ACKNOWLEDGMENTS

We are pleased to acknowledge many people at SLAC for their assistance in setting up and running this experiment. In particular, we thank John Mark and the SLAC target group for design, construction, and maintenance of the targets; Dave Sherden for help with the online software, and Robert Eisele and the Spectrometer Facilities Group for assistance in setting up the detectors.

## REFERENCES

1. T. Narita, Progress in Theoretical Physics **42**, 1336 (1969);  
A. L. Licht and A. Pagnamenta, Phys. Rev. **D4**, 2810 (1971).
2. F. Iachello *et al.*, Phys. Lett. **43B**, 191 (1973).
3. S. Blatnik and N. Zovko, Acta Physica Austriaca **39**, 62 (1974).
4. F. Felst, DEST preprint 73/56, unpublished.
5. G. Hohler *et al.*, Nucl. Phys. **B114**, 505 (1976).
6. J. G. Korner, M. Kuroda, Phys. Rev. **D16**, 2165 (1977).
7. S. D. Drell and T. M. Yan, Phys. Rev. Lett. **24**, 181 (1970).
8. S. J. Brodsky and B. Chertok, Phys. Rev. **D14**, 3003 (1976).
9. C. R. Ji and A. F. Sill, Phys. Rev. **D34**, 3350 (1986);  
V. L. Chernyak and I. R. Zhitnitsky, Nucl. Phys. **B246**, 52 (1984);  
S. Brodsky and G. P. Lepage, Phys Scripta **23**, 945 (1981);  
Phys. Rev. **D22**, 2157 (1980);  
A. Duncan and A. H. Mueller, Phys. Lett. **90B**, 159 (1980).
10. M. Gari and W. Krumpelmann, Phys. Lett. **B173**, 10 (1986);  
Z. Phys. A322, 689 (1985).
11. V. A. Nesterenko and A. V. Radyushkin, Yad. Fiz. **39**, 1287 (1984);  
V. Radyushkin, Acta Physica Polonica **B15**, 403 (1984).
12. V. A. Matveev, R. M. Muradyan, A. N. Tavkhelidze, Lett. Nuovo Cim. **7**, 719  
(1973);  
S. J. Brodsky at G. R. Farrar, Phys. Rev. Lett. **31**, 1153 (1973).
13. J. P. Vary, Nucl. Phys. **A418**, 195 (1984).
14. L. L. Frankfurt and M. I. Strikman, Physics Reports **160**, 235 (1988).

15. C. Ciofi degli Atti *et al.*, Nucl. Phys. **A463**, 127 (1987).
16. P. E. Bosted *et al.*, Phys. Rev. Lett. **49**, 1380 (1982).
17. G. B. West, Phys. Rep. **18**, 263 (1975);  
S. A. Gurvitz and A. S. Rinat, Phys. Rev. **C35**, 696 (1987).
18. J. J. Aubert *et al.*, Phys. Lett. **123B**, 275 (1983);  
G. Bari *et al.*, Phys. Lett. **163B**, 282 (1985);  
A. Bodek *et al.*, Phys. Rev. Lett. **50**, 1431 (1983);  
R. G. Arnold *et al.*, Phys. Rev. Lett. **52**, 727 (1984);  
G. Bari *et al.*, Phys. Lett. **163B**, 282 (1985);  
J. Ashman *et al.*, Phys. Lett. **202B**, 603 (1988).
19. A. Bodek and J. L. Ritchie, Phys. Rev. **D23**, 1070 (1981);  
**D24**, 1400 (1981).
20. L. Mo, SLAC Technical Note SLAC TN-65-40 (1965).
21. S. Stein *et al.*, Phys. Rev. **D12**, 1884 (1975).
22. M. D. Mestayer, SLAC-214, Stanford University Ph.D. thesis (1978),  
unpublished.
23. R. Walker *et al.*, Phys. Lett. **B224**, 353 (1989);  
California Institute of Technology Ph.D. thesis (1989), to be published.
24. R. B. Stewart and H. M. Roder, "Properties of Normal and Parahydrogen,"  
in *Technology and Uses of Liquid Hydrogen*, (Pergamon Press, NY, 1964),  
p. 379-404;  
Cryogenic Data Center Memorandum M4, Cryogenic Division of National  
Bureau of Standards, Boulder, Colorado.
25. SLAC Users Handbook, and E. A. Taylor, SLAC Technical Note TN-71-26.
26. A. Bodek *et al.*, Phys. Rev. **20**, 1471 (1979).

27. W. Schutz *et al.*, Phys. Rev. Lett. **38**, 259 (1977).
28. Y. S. Tsai, SLAC preprint SLAC-PUB-848 Rev. (1971);  
see also L. W. Mo and Y. S. Tsai, Rev. Mod. Phys. **41**, 205 (1969).
29. R. G. Arnold *et al.*, Phys. Rev. Lett. **57**, 174 (1986).
30. L. Whitlow, SLAC Report-357, Stanford University Ph.D. thesis (1990).
31. Private communication, Lisa Clogher.
32. A. A. Akhundov, D. Yu. Bardin, and N. M. Shumeiko, Sov. J. Nucl. Phys. **26**  
(6), 660 (1978); JINR preprint E2-10205;  
A. A. Akhundov, D. Yu. Bardin, and W. Lohmann, JINR preprint E2-86-104;  
D. Yu. Bardin and N. M. Shumeiko, JINR preprint P2-10873.
33. S. Dasu, University of Rochester Ph.D. thesis (1988).
34. W. P. Schutz *et al.*, Phys. Rev Lett . **38**, 259 (1977);  
and R. Arnold, private communication.
35. K. Holinde and R. Machleidt, Nucl. Phys. **A256**, 479 (1976); **A256**, 497  
(1976).
36. R. V. Reid, Jr., Ann. Phys. (NY) **50**, 411 (1968).
37. M. Bernheim *et al.*, Nucl. Phys. **A365**, 349 (1981).
38. M. Lacombe *et al.*, Phys. Lett. **101B**, 139 (1981).
39. E. Lomen and H. Feshbach, Ann. Phys. (NY) **48**, 94 (1968).
40. I. J. McGee, Phys. Rev. **161**, 1640 (1967)  
and L. Durand, Phys. Rev. **123**, 1 393 (1961),  
as presented in W. Bartel *et al.*, Nucl. Phys. **B58**, 429 (1973).
41. P. E. Bosted *et al.*, Phys. Rev. Lett. **49**, 1380 (1982);  
C. Ciofi degli Atti *et al.*, Nucl. Phys. **A463**, 127 (1987);  
S. A. Gurvitz and A. S. Rinat, Phys. Rev. **C35**, 696 (1987),  
and references therein.

42. R. Machleidt, K. Holinde, and C. Elster, *Phys. Rep.* **149**, 1 (1987).
43. B. Parker *et al.*, *Phys. Rev.* **C34**, 2354 (1986);  
 B. Quinn *et al.*, *Phys. Rev.* **C37**, 1609 (1988);  
 A. S. Esauslov *et al.*, *Yad. Piz.* **45**, 410 (1987);  
 R. Arnold *et al.*, *Phys. Rev. Lett.* **61**, 806 (1988).
44. J. M. Laget, *Can. J. Phys.* **62**, 1046 (1984), and private communication.
45. H. Arenhövel, *Nucl. Phys.* **A384**, 287 (1982), and private communication.
46. M. M. Sargsian, L. L. Frankfurt, and M. I. Strikman, *Z. Phys.* **A335**, 431 (1990).
47. W. Albrecht *et al.*, *Phys. Lett.* **26B**, 642 (1968);  
 R. J. Budnitz *et al.*, *Phys. Rev.* **173**, 1357 (1968);  
 W. Bartel *et al.*, *Nucl. Phys.* **B58**, 429 (1973).
48. J. R. Dunning *et al.*, *Phys. Rev.* **141**, 1286 (1966);  
 K. Hanson *et al.*, *Phys. Rev.* **D8**, 1305 (1973);  
 C. W. Akerlof *et al.* *Phys. Rev.* **135B**, 810 (1964);  
 E. B. Hughes *et al.*, *Phys. Rev.* **139B**, 358 (1965).
49. K. J. Barnes, P. Carruthers, and F. von Hippel, *Phys. Rev. Lett.* **14**, 82 (1965).
50. P. Bosted, IV Conf. on the Intersections of Particle and Nuclear Physics, Tucson, AZ, 1991, to be published.
51. S. Brodsky and G. Farrar, *Phys. Rev.* **D11**, 1309 (1975).
52. G. Farrar and D. Jackson, *Phys. Rev. Lett.* **35**, 1416 (1975).
53. L. Frankfurt and M. Strikman, *Phys. Rep.* **76**, 215 (1981);  
*Nucl. Phys.* **B250**, 143 (1985).
54. J. Vary in *Proc. VIII Int. Seminar on High Energy Physics Problems, Vol. II*, Dubna, USSR, June 86, p. 27.

55. J. Vary *et al.*, Phys. Rev. **C33**, 1062 (1986).
56. I. Schmidt and R. Blankenbecler, Phys. Rev. **D15**, 3321 (1977); **D16**, 1318 (1977);  
R. Blankenbecler in *Recent Developments in Particle and Field Theory*,  
Tubingen, 1977, Walter Dittrich, Ed., (Friedr. Vieweg & Sohn, Braunschweig  
/Wiesbaden, 1979).
57. L. L. Frankfurt and M. I. Strikman, Phys. Lett. **69B**, 93 (1977); Nucl. Phys.  
**B148**, 107 (1979).
58. R. Blankenbecler and S. J. Brodsky, Phys. Rev. **D10**, 2973 (1974).
59. S. D. Drell and T. M. Yan, Phys. Rev. Lett. **24**, 181 (1970).
60. G. B. West, Phys. Rev. Lett. **24**, 1206 (1970).
61. R. Arnold *et al.*, Phys. Rev. Lett. **35**, 776 (1975).

## FIGURE CAPTIONS

1. Monte Carlo simulation of the experimentally measured quasi-elastic peak, including radiative effects at two values of  $Q^2$ .
2. Plan view of End Station A showing, from left to right, the incident beam going through the toroids, the target assembly, and the 20-GeV spectrometer with its detectors.
3. Shower Counter spectrum for two values of spectrometer momentum. The arrow indicates the cut separating electrons from pions.
4. The  $\phi$  acceptance of the spectrometer as a function of  $\delta p/p$  for three values of  $\delta\theta$ .
5. The  $\phi$  acceptance of the spectrometer as a function of  $\delta\theta$  for three values of  $\delta p/p$ . The cause of the humped shape is described in the text.
6. The experimental elastic cross section from hydrogen at  $Q^2 = 2.5 \text{ (GeV/c)}^2$  compared to the Monte Carlo Model. Excellent agreement is found at both the peak and radiative tails.
7. Double differential cross sections per nucleus as a function of missing mass and scattered electron energy for different effective beam energies for (a) proton and (b) deuteron.
8. Scaling of the structure function  $\nu W_2(x, Q^2)$ .  $\nu W_2$  is plotted versus (a) the Nachmann variable  $\xi$ , and (b) the Bloom-Gilman scaling variable  $\omega'$ .
9. Monte-Carlo generated inelastic deuterium events that are in the quasi-elastic peak ( $0.7 \leq W^2 \leq 1.1 \text{ GeV}^2$ ). The percentage of events is plotted versus their missing-mass squared in the struck nucleon rest frame ( $W_{\text{gen}}^2$ ) for two values of  $Q^2$ .

10. Monte-Carlo generated inelastic deuterium events that are in the quasi-elastic peak ( $0.7 \leq W^2 \leq 1.1 \text{ GeV}^2$ ). The percentage of events is plotted vs. the Fermi momentum of the struck nucleon for two values of  $Q^2$ . Also shown (dotted curve) is the unbiased Fermi momentum distribution.
11. Experimental deuterium cross sections before radiative corrections compared to the Monte Carlo Model. Shown are the smeared proton elastic (dashed) and inelastic (dotted) Monte Carlo calculations, with the best-fit sum of proton plus neutron, smeared elastic plus inelastic (solid).
12. The fractional difference between the experimental deuterium cross section and the Monte Carlo model.
13. Ratios of deuterium cross sections to the two-parameter fits using the  $y$ -scaling method with the Paris wave function and no correction factor [ $C(y) = 1$ ].
14. Ratios of deuterium cross sections to the PWIA model of McGee-Durand [40] for five values of the scaling variable  $y$ , using the Paris potential. Shown are data from this experiment and several previous experiments at both forward and backward angles [43]. The solid curves are the full calculations of Laget [44] and the dashed curves are those of Arenhövel [45]. The calculations are independent of electron scattering angle.
15. Same as for Fig. 13, except with  $C(y) = 1 + 1.5 |y| + 1.5 y^2$ .
16. Experimental deuterium cross sections compared with the  $y$ -scaling model. The dashed lines are the quasi-elastic contributions, the dot-dashed lines are the inelastic contributions, and the solid lines are the sum. The Paris potential was used with  $C(y) = 1 + 1.5 |y| + 1.5 y^2$ .
17.  $\sigma_n^{\text{el}}/\sigma_p^{\text{el}}$  as a function of  $Q^2$  from this experiment (solid circles). The inner error bars include systematic and statistical uncertainties, combined

in quadrature. The outer error bars also include model dependence uncertainties, added in quadrature. Also shown are the results of previous measurements by Albrecht et al., (open diamonds), Budnitz et al., (crosses) and Bartel et al., (open squares) [47]. The Vector Meson Dominance fits of Hohler (dashdot curve) [5], and Korner & Kuroda (solid curve) [6] are also shown, along with the hybrid model of Gari and Krumpelmann (dashed curve) [10]. The dotted curve uses experimental values of the proton form factors [23], the dipole for  $G_M^N$  and  $G_E^N = 0$ . This curve is almost identical to Form Factor Scaling.

18. The ratio of spectrometer acceptance for the Dummy aluminum target, compared to the full deuterium target averaged overall spectrometer momentum, as a function of  $\delta\theta$ . Both ends of the Dummy target are within the acceptance only in the middle of the central region.
19. Ratio of cross sections per nucleon of aluminum compared to deuterium, as a function of  $W^2$ .
20. Deuterium experimental cross sections near threshold, as a function of  $W_d^2$ . A rough fit to the data described in the text is also shown.
21. Experimental  $\nu W_2^d/x_d$  near threshold as a function of  $(1 - x_d)$ , for this experiment at  $Q^2 = 8(\text{GeV}/c)^2$ , and for previous experiments [34] at lower  $Q^2$ . Also shown is a power-law fit to the data described in the text.
22. Experimental  $\nu W_2^d/\xi$  near threshold as a function of  $\xi_{max} - \xi$ , for this experiment at  $Q^2 = 8(\text{GeV}/c)^2$ , and for previous experiments [34] at lower  $Q^2$ . Also shown are power-law fits to the data in the region  $0.05 \leq \xi_{max} - \xi \leq 0.17$ , described in the text.
23. The ratio of inelastic- to-elastic deuterium structure functions versus  $Q^2$ . The straight lines show the approximate asymptotic behavior for each kinematic offset from the deuteron mass.

TABLE I. Beam parameters.

Beam energy, nominal (GeV)	9.761	12.589	15.742	17.328	18.497	21.001
Beam energy, actual (GeV)	9.750	12.571	15.736	17.307	18.482	21.005
$Q_{\text{elastic}}^2$ , actual $[(\text{GeV}/c)^2]$	2.495	3.989	5.996	7.109	7.988	10.004
Energy slits, full width (%)	0.25	0.40	0.25	0.50	0.30	0.40
Beam energy spread (%)	$\pm 0.19$	$\pm 0.16$	$\pm 0.19$	$\pm 0.20$	$\pm 0.19$	$\pm 0.14$
Resolution $W^2$ (GeV <sup>2</sup> )	$\pm 0.03$	$\pm 0.03$	$\pm 0.05$	$\pm 0.05$	$\pm 0.05$	$\pm 0.04$
Average current (ma)	8	18	20	40	23	28

TABLE II. Systematic uncertainties for cross sections and cross section ratios. Some contributions to the individual errors cancel in the ratios, while others add in quadrature.

Quantity	Uncertainty	$d\sigma/d\Omega E'$ (%)	$\sigma_{Al}/\sigma_d$ (%)	$\sigma_d/\sigma_p$ (%)
Beam				
Angle	$\pm 0.2$ mr	$\pm 1.4$	$\pm 1.4$	$\pm 1.4$
Energy	$\pm 0.1$ %	$\pm 0.6$	$\pm 0.4$	$\pm 0.4$
Charge	$\pm 0.5$ %	$\pm 0.5$	$\pm 0.3$	$\pm 0.3$
Target density				
Beam effects	$\leq \pm 1$ %	$\leq \pm 1$	$\leq \pm 0.5$	$\leq \pm 0.7$
Thickness	--	$\leq \pm 0.5$	$\leq \pm 2$	$\leq \pm 0.5$
Temperature	$\leq \pm 0.4$ %	$\leq \pm 0.4$	$\leq \pm 0.4$	$\leq \pm 0.4$
Acceptance	$\pm 3$ %	$\pm 3$	$\pm 3$	$\pm 1$
Spectrometer				
Angle	$\pm 0.2$ mr	$\pm 1.4$	$\pm 0.6$	$\pm 0.6$
Momentum	$\pm 0.1$ %	$\pm 0.6$	$\pm 0.2$	$\pm 0.2$
Chamber efficiency	$\pm 1.0$ %	$\pm 1.0$	$\pm 0.5$	$\pm 0.5$
Deadtime	$\pm 0.5$ %	$\pm 0.5$	$\leq \pm 0.5$	$\leq \pm 0.3$
Radiative effects peak- ing approximation	$\pm 2.0$ %	$\pm 2.0$	$\pm 1.5$	$\pm 1.0$
Total		$\leq \pm 5$	$\leq \pm 5$	$\leq \pm 2.3$

TABLE III. Target parameters.

	Deuterium	Hydrogen	Dummy
Length along beam (cm)	30.25	30.24	30.48
Diameter (cm)	8.89	8.89	8.89
Each endcap, aluminum (cm)	0.0127	0.0127	0.191
Density (gm/cm <sup>3</sup> )	0.168	0.0694	2.70
Radiation lengths (fraction)	0.0415	0.0342	0.0430

TABLE IV. Elastic cross section compared to model and to previous experiments. The ratio of this experiment to the fit of Gari and Krumpelmann [10] is shown in column four. The reduced form factor is shown in column five for this experiment and in column six for previous experiments [23,28].

E	$Q^2$	$Q^4 G_M / \mu_p$			
		This Experiment (nb/sr)	Gari model	This Experiment	Previous Experiments
9.750	2.495	$7.7000 \pm 0.0500$	$0.966 \pm 0.006$	$0.307 \pm 0.001$	$0.313 \pm .003$
12.571	3.990	$1.1170 \pm 0.0110$	$0.946 \pm 0.009$	$0.357 \pm 0.002$	$0.370 \pm .004$
15.736	5.996	$0.1795 \pm 0.0024$	$0.967 \pm 0.013$	$0.384 \pm 0.003$	$0.395 \pm .004$
18.482	7.988	$0.0448 \pm 0.0010$	$0.978 \pm 0.022$	$0.389 \pm 0.004$	$0.401 \pm .004$
21.005	10.004	$0.0145 \pm 0.0005$	$1.002 \pm 0.034$	$0.390 \pm 0.007$	$0.395 \pm .005$

TABLE V. Ratio of elastic cross sections measured at different offsets from the center of the spectrometer to the cross section measured at the center.

$Q^2$	-2% Offset	-1% Offset	+1% Offset	+2% Offset
2.5	$0.996 \pm 0.06$	$0.990 \pm 0.015$	$0.997 \pm 0.017$	$0.969 \pm 0.056$
4.0	$0.995 \pm 0.10$	$0.988 \pm 0.027$	$0.951 \pm 0.025$	$0.893 \pm 0.066$
6.0	$1.017 \pm 0.05$	$1.006 \pm 0.025$	$0.987 \pm 0.028$	$0.999 \pm 0.042$
8.0	$0.983 \pm 0.08$	$0.982 \pm 0.042$	$1.005 \pm 0.045$	
Average	$0.993 \pm 0.032$	$0.992 \pm 0.011$	$0.985 \pm 0.012$	$0.968 \pm 0.030$

TABLE VI.A. For energy = 9.744, the  $ed$  and  $ep$  cross sections per nucleus and the ratio of aluminum-to-deuterium cross sections per nucleon.

$E'$ (GeV)	$W^2$ (GeV <sup>2</sup> )	$\frac{d^2\sigma_d}{d\Omega dE'} (nb/GeV/sr)$	$\frac{d^2\sigma_p}{d\Omega dE'} (nb/GeV/sr)$	$\frac{\sigma_{Al}}{\sigma_d}$
8.972	-0.328	0.132±0.108		
8.961	-0.304	0.167±0.093		
8.949	-0.278	0.116±0.082		
8.938	-0.254	0.153±0.072		
8.926	-0.228	0.164±0.067		
8.915	-0.204	0.146±0.063		
8.903	-0.178	0.201±0.060		5.26±4.23
8.892	-0.154	0.182±0.056		
8.880	-0.128	0.191±0.055		
8.869	-0.104	0.363±0.063		
8.857	-0.078	0.297±0.053		
8.846	-0.054	0.291±0.050		3.71±1.38
8.834	-0.027	0.422±0.054		
8.823	-0.004	0.363±0.052		
8.811	0.023	0.405±0.053		
8.800	0.047	0.564±0.068		
8.788	0.073	0.619±0.065		4.11±0.69
8.777	0.097	0.698±0.072		
8.765	0.123	0.735±0.082		
8.754	0.147	1.01±0.10		
8.742	0.173	1.02±0.08		
8.731	0.197	1.08±0.12		3.85±0.38
8.719	0.223	1.50±0.12		
8.708	0.247	1.51±0.10		
8.696	0.273	1.68±0.11		
8.685	0.297	2.14±0.13		
8.673	0.323	2.35±0.13		2.85±0.21
8.662	0.347	2.43±0.15		
8.650	0.373	3.13±0.16		
8.639	0.397	3.48±0.21		
8.627	0.423	4.51±0.20		
8.616	0.447	4.88±0.21		1.94±0.12
8.604	0.473	5.90±0.24		
8.593	0.497	6.94±0.27		
8.581	0.523	9.01±0.32		
8.570	0.547	9.69±0.37		
8.559	0.571	12.2±0.4		1.27±0.06
8.547	0.597	15.3±0.4		
8.536	0.621	17.6±0.6		
8.524	0.647	21.7±0.7		

*Continued*

TABLE VI.A. Continued. For energy = 9.744, the  $ed$  and  $ep$  cross sections per nucleus and the ratio of aluminum-to-deuterium cross sections per nucleon.

$E'$ (GeV)	$W^2$ (GeV <sup>2</sup> )	$\frac{d^2\sigma_d}{d\Omega dE'}$ (nb/GeV/sr)	$\frac{d^2\sigma_p}{d\Omega dE'}$ (nb/GeV/sr)	$\frac{\sigma_{Al}}{\sigma_d}$
8.513	0.671	25.3±0.8		
8.500	0.697	29.7±0.7		0.59±0.03
8.489	0.721	35.5±1.0		
8.477	0.747	40.5±0.8		
8.466	0.771	45.2±0.8		
8.454	0.797	49.0±1.0		
8.443	0.821	51.1±0.9		0.41±0.02
8.431	0.847	54.1±1.2		
8.420	0.871	52.1±0.9		
8.408	0.897	48.2±0.9		
8.397	0.921	44.6±0.8		
8.385	0.947	40.7±0.8		0.46±0.02
8.374	0.971	38.7±0.8		
8.362	0.997	33.8±0.7		
8.351	1.021	31.8±0.8		
8.339	1.048	28.4±0.6		
8.328	1.071	27.4±0.7		0.79±0.04
8.316	1.098	25.9±0.7		
8.305	1.121	25.8±0.6	1.2±0.9	
8.293	1.148	24.1±0.6	1.1±0.6	
8.282	1.172	24.9±0.6	2.2±0.6	
8.270	1.198	25.1±0.7	5.4±0.6	1.24±0.05
8.259	1.222	26.6±0.8	5.6±0.8	
8.247	1.248	27.8±0.9	7.2±0.7	
8.236	1.272	30.8±0.8	9.3±0.8	
8.224	1.298	30.7±0.8	12.6±0.9	
8.213	1.322	33.5±0.9	16.0±0.8	1.04±0.05
8.201	1.348	35.9±0.9	18.7±0.9	
8.190	1.372	38.6±1.1	23.2±1.0	
8.178	1.398	40.4±1.1	29.1±1.4	
8.167	1.422	42.2±1.1	33.9±1.1	
8.155	1.448	43.8±1.2	36.8±1.5	0.89±0.04
8.144	1.472	43.6±1.2	40.0±1.4	
8.133	1.496	46.9±1.5	39.7±1.4	
8.121	1.522	48.5±1.4	37.4±1.4	
8.110	1.546	47.4±1.8	36.6±1.3	
8.098	1.572	48.6±1.5	35.4±1.1	0.78±0.03
8.087	1.596	47.9±1.5	33.6±1.1	
8.075	1.622	50.6±1.6	31.0±1.1	
8.064	1.646	52.7±1.7	33.5±1.1	
8.052	1.672	50.1±1.7	30.2±1.2	

Continued

TABLE VI.A. Continued. For energy = 9.744, the  $ed$  and  $ep$  cross sections per nucleus and the ratio of aluminum-to-deuterium cross sections per nucleon.

$E'$ (GeV)	$W^2$ (GeV <sup>2</sup> )	$\frac{d^2\sigma_d}{d\Omega dE'} (nb/GeV/sr)$	$\frac{d^2\sigma_p}{d\Omega dE'} (nb/GeV/sr)$	$\frac{\sigma_{Al}}{\sigma_d}$
8.041	1.696	48.7±2.1	29.8±1.1	0.89±0.04
8.029	1.722	51.1±1.8	33.0±1.2	
8.018	1.746	51.9±2.3	29.1±1.1	
8.006	1.772	55.2±2.2	32.3±1.4	
7.995	1.796	50.3±1.9	31.1±1.3	
7.983	1.822	56.8±2.4	34.2±1.3	0.99±0.05
7.972	1.846	59.1±2.0	30.9±1.2	
7.960	1.872	54.8±1.9	34.5±1.4	
7.949	1.896	59.1±2.0	36.7±1.4	
7.937	1.922	60.9±2.0	37.3±1.3	
7.926	1.946	58.0±2.0	35.7±1.4	0.97±0.04
7.914	1.972	61.0±2.1	36.4±1.4	
7.903	1.996	62.7±2.1	35.3±1.3	
7.891	2.022	63.1±2.5	39.2±1.4	
7.879	2.046	67.7±2.6	42.1±1.5	
7.867	2.072	70.7±2.6	41.9±1.9	1.05±0.05
7.856	2.096	72.8±2.7	47.0±2.6	
7.844	2.122	73.0±3.1	54.7±2.3	
7.833	2.146	80.4±3.7	56.1±3.4	
7.821	2.173	83.8±3.2	62.7±2.6	
7.810	2.196	84.2±4.1	68.8±2.8	0.91±0.06
7.798	2.223	86.6±4.9	68.8±3.2	
7.787	2.247	86.7±4.3	64.8±3.2	
7.775	2.273	87.0±4.2	69.9±3.2	
7.764	2.297	96.4±4.1	59.1±2.9	
7.752	2.323	85.3±3.8	61.0±3.5	0.85±0.07
7.741	2.347	97.5±4.7	64.2±3.1	
7.730	2.371	82.9±4.9	58.7±3.0	
7.718	2.397	84.5±4.0	59.3±3.0	
7.707	2.421	93.4±5.1	58.6±3.4	0.91±0.08

TABLE VI.B. For energy = 12.565, the  $ed$  and  $ep$  cross sections per nucleus and the ratio of aluminum-to-deuterium cross sections per nucleon.

$E'$ (GeV)	$W^2$ (GeV <sup>2</sup> )	$\frac{d^2\sigma_d}{d\Omega dE'} (nb/GeV/sr)$	$\frac{d^2\sigma_p}{d\Omega dE'} (nb/GeV/sr)$	$\frac{\sigma_{Al}}{\sigma_d}$
10.992	-0.365	0.0375±0.0830		
10.977	-0.331	0.120±0.069		
10.963	-0.299	0.0206±0.0677		
10.948	-0.265	0.0972±0.0636		
10.933	-0.231	0.0685±0.0546		
10.919	-0.200	0.108±0.050		
10.904	-0.166	0.136±0.044		
10.890	-0.134	0.208±0.045		
10.875	-0.100	0.160±0.037		3.30±1.89
10.860	-0.066	0.119±0.035		
10.846	-0.034	0.150±0.033		
10.831	0.000	0.169±0.035		
10.817	0.031	0.201±0.032		
10.802	0.065	0.258±0.036		4.12±0.99
10.788	0.097	0.360±0.038		
10.773	0.131	0.292±0.034		
10.758	0.165	0.370±0.036		
10.744	0.196	0.457±0.053		
10.729	0.230	0.506±0.052		2.32±0.35
10.715	0.262	0.572±0.045		
10.700	0.296	0.690±0.057		
10.685	0.330	0.776±0.064		
10.671	0.361	0.931±0.058		
10.656	0.395	1.20±0.07		1.37±0.15
10.642	0.427	1.32±0.09		
10.627	0.461	1.69±0.09		
10.613	0.493	1.92±0.09		
10.597	0.527	2.25±0.10		
10.582	0.560	2.50±0.11		0.87±0.08
10.568	0.592	2.93±0.11		
10.553	0.626	3.37±0.12		
10.539	0.658	3.97±0.18		
10.524	0.692	4.59±0.14		
10.509	0.726	5.11±0.19		0.63±0.05
10.495	0.757	5.75±0.15		
10.480	0.791	5.96±0.19		
10.466	0.823	6.23±0.17		
10.451	0.857	6.02±0.24		
10.436	0.891	6.31±0.17		0.51±0.04

*Continued*

TABLE VI.B.Continued. For energy = 12.565, the  $ed$  and  $ep$  cross sections per nucleus and the ratio of aluminum-to-deuterium cross sections per nucleon.

$E'$ (GeV)	$W^2$ (GeV <sup>2</sup> )	$\frac{d^2\sigma_d}{d\Omega dE'} (nb/GeV/sr)$	$\frac{d^2\sigma_p}{d\Omega dE'} (nb/GeV/sr)$	$\frac{\sigma_{Al}}{\sigma_d}$
10.422	0.922	6.06±0.19		
10.407	0.956	5.56±0.15		
10.393	0.988	4.99±0.16		
10.378	1.022	5.00±0.15		
10.364	1.054	4.60±0.15		0.74±0.06
10.349	1.087	4.69±0.16		
10.334	1.121	4.59±0.16	0.36±0.18	
10.320	1.153	4.56±0.17	0.44±0.17	
10.305	1.187	4.54±0.16	0.78±0.12	
10.291	1.219	4.89±0.16	0.76±0.12	1.03±0.10
10.276	1.253	4.92±0.15	1.56±0.18	
10.261	1.286	5.49±0.17	2.09±0.16	
10.247	1.318	5.60±0.18	2.64±0.17	
10.232	1.352	6.12±0.17	3.64±0.19	
10.218	1.384	6.57±0.17	4.46±0.23	1.05±0.08
10.203	1.418	6.78±0.18	5.25±0.20	
10.189	1.449	6.99±0.19	5.14±0.20	
10.174	1.483	7.35±0.22	5.54±0.21	
10.159	1.517	7.54±0.20	5.31±0.23	
10.145	1.549	8.08±0.22	5.48±0.21	0.96±0.07
10.130	1.583	8.34±0.22	5.20±0.20	
10.116	1.614	8.76±0.23	5.52±0.21	
10.101	1.648	8.55±0.24	5.39±0.24	
10.086	1.682	9.44±0.27	5.86±0.23	
10.072	1.714	9.23±0.31	5.99±0.23	0.91±0.07
10.057	1.748	10.0±0.3	6.2±0.2	
10.043	1.780	9.81±0.35	6.83±0.26	
10.028	1.813	9.91±0.29	7.42±0.29	
10.014	1.845	11.0±0.3	7.2±0.3	
9.999	1.879	10.9±0.3	6.9±0.3	0.95±0.09
9.984	1.913	12.0±0.4	7.3±0.3	
9.970	1.945	13.1±0.4	7.2±0.3	
9.955	1.979	12.9±0.5	7.6±0.4	
9.940	2.010	13.5±0.4	8.5±0.4	
9.925	2.044	13.6±0.5	8.6±0.4	0.79±0.08

TABLE VI.C. For energy = 15.730, the  $ed$  and  $ep$  cross sections per nucleus and the ratio of aluminum-to-deuterium cross sections per nucleon.

$E'$ (GeV)	$W^2$ (GeV <sup>2</sup> )	$\frac{d^2\sigma_d}{d\Omega dE'} \text{ (nb/GeV/sr)}$	$\frac{d^2\sigma_p}{d\Omega dE'} \text{ (nb/GeV/sr)}$	$\frac{\sigma_{Al}}{\sigma_d}$
13.139	-0.537	0.0265±0.0155		
13.121	-0.494	0.00886±0.00981		
13.102	-0.450	0.0160±0.0093		
13.083	-0.405	0.0347±0.0094		
13.065	-0.362	0.0323±0.0081		
13.046	-0.318	0.0290±0.0071		
13.027	-0.273	0.0375±0.0066		
13.009	-0.230	0.0400±0.0060		
12.990	-0.186	0.0384±0.0059		
12.972	-0.143	0.0402±0.0053		3.98±2.19
12.953	-0.098	0.0468±0.0062		
12.934	-0.053	0.0551±0.0055		
12.915	-0.011	0.0612±0.0056		
12.896	0.034	0.0801±0.0063		
12.877	0.079	0.0836±0.0064		3.55±1.00
12.859	0.121	0.0953±0.0070		
12.840	0.166	0.116±0.007		
12.821	0.211	0.146±0.008		
12.803	0.253	0.149±0.008		
12.784	0.298	0.170±0.008		1.09±0.42
12.765	0.343	0.213±0.009		
12.747	0.385	0.242±0.010		
12.728	0.430	0.286±0.010		
12.709	0.475	0.340±0.012		
12.691	0.517	0.379±0.011		0.99±0.18
12.672	0.562	0.442±0.013		
12.653	0.607	0.518±0.013		
12.635	0.649	0.599±0.014		
12.616	0.694	0.647±0.015		
12.597	0.739	0.720±0.015		0.76±0.10
12.579	0.781	0.798±0.019		
12.560	0.826	0.856±0.017		
12.541	0.871	0.907±0.018		
12.523	0.913	0.954±0.021		
12.504	0.958	0.888±0.018		0.85±0.09
12.485	1.003	0.925±0.020		
12.467	1.045	0.891±0.022		
12.448	1.090	0.922±0.018		
12.429	1.135	0.872±0.020	0.055±0.022	
12.411	1.177	0.920±0.019	0.030±0.016	0.99±0.11

*Continued*

TABLE VI.C. Continued. For energy = 15.730, the  $ed$  and  $ep$  cross sections per nucleus and the ratio of aluminum-to-deuterium cross sections per nucleon.

$E'$ (GeV)	$W^2$ (GeV <sup>2</sup> )	$\frac{d^2\sigma_d}{d\Omega dE'} (nb/GeV/sr)$	$\frac{d^2\sigma_p}{d\Omega dE'} (nb/GeV/sr)$	$\frac{\sigma_{Al}}{\sigma_d}$
12.392	1.222	0.946±0.020	0.052±0.018	
12.373	1.267	1.00±0.02	0.11±0.02	
12.355	1.309	1.06±0.02	0.20±0.02	
12.336	1.354	1.12±0.02	0.29±0.03	
12.318	1.397	1.18±0.03	0.42±0.03	1.21±0.09
12.299	1.441	1.26±0.03	0.59±0.03	
12.280	1.486	1.29±0.03	0.77±0.04	
12.262	1.529	1.37±0.03	0.79±0.04	
12.242	1.574	1.45±0.03	0.80±0.03	
12.223	1.618	1.57±0.03	0.84±0.04	1.14±0.08
12.205	1.661	1.62±0.03	0.91±0.03	
12.186	1.706	1.73±0.04	1.01±0.04	
12.167	1.750	1.88±0.04	1.02±0.04	
12.149	1.793	1.95±0.04	1.09±0.04	
12.130	1.838	2.07±0.05	1.28±0.04	1.00±0.06
12.111	1.882	2.21±0.05	1.26±0.04	
12.093	1.925	2.31±0.05	1.34±0.05	
12.074	1.970	2.56±0.05	1.39±0.05	
12.055	2.014	2.54±0.06	1.58±0.06	
12.037	2.057	2.69±0.06	1.66±0.05	0.94±0.06
12.018	2.102	2.85±0.09	1.69±0.05	
11.999	2.147	2.81±0.07	1.93±0.06	
11.981	2.189	3.17±0.09	2.42±0.07	
11.962	2.234	3.33±0.11	2.85±0.08	0.90±0.08
11.943	2.279		2.87±0.11	
11.925	2.321		3.04±0.10	
11.906	2.366		2.96±0.09	
11.887	2.411		2.67±0.09	
11.869	2.453		2.52±0.09	
11.850	2.498		2.61±0.09	
11.831	2.543		2.64±0.10	
11.813	2.585		2.50±0.10	
11.794	2.630		2.66±0.12	
11.775	2.675		2.74±0.11	
11.757	2.717		2.91±0.12	
11.738	2.762		3.32±0.16	
11.719	2.807		3.90±0.17	
11.701	2.849		3.87±0.19	

TABLE VI.D. For energy = 17.301, the  $ed$  and  $ep$  cross sections per nucleus and the ratio of aluminum-to-deuterium cross sections per nucleon.

$E'$ (GeV)	$W^2$ (GeV <sup>2</sup> )	$\frac{d^2\sigma_d}{d\Omega dE'} (nb/GeV/sr)$	$\frac{d^2\sigma_p}{d\Omega dE'} (nb/GeV/sr)$	$\frac{\sigma_{Al}}{\sigma_d}$
14.990	-2.664	0.00002±.00001		
14.943	-2.551	0.00004±.00002		
14.897	-2.440	0.00004±.00002		0.00±9.32
14.850	-2.327	0.00014±.00003		3.73±3.73
14.803	-2.214	0.00005±.00003		37.27±22.36
14.756	-2.101	0.00010±.00004		7.45±7.45
14.710	-1.990	0.00026±.00006		11.18±4.66
14.663	-1.877	0.00044±.00009		8.39±3.73
14.616	-1.764	0.00070±.00012		2.80±1.86
14.341	-1.105	0.00365±.00298		
14.319	-1.052	0.00272±.00398		
14.296	-0.996	0.00432±.00363		
14.274	-0.944	0.00442±.00359		
14.251	-0.888	0.00645±.00370		
14.229	-0.835	0.00902±.00409		
14.206	-0.780	0.00362±.00402		
14.184	-0.727	0.00596±.00420		
14.162	-0.674	0.00697±.00442		
14.139	-0.619	0.0123±.0047		
14.117	-0.566	0.00963±.00490		
14.094	-0.511	0.00423±.00517		
14.072	-0.458	0.0234±.0061		
14.049	-0.402	0.0186±.0074		
14.027	-0.349	0.0111±.0076		
14.004	-0.294	0.0134±.0087		
13.982	-0.241	0.0185±.0109		
13.960	-0.188	0.0351±.0118		
13.937	-0.133	0.0356±.0171		
13.915	-0.080	0.0368±.0172		
13.892	-0.025	0.0234±.0143		
13.870	0.028	0.0333±.0168		
13.847	0.084	0.0493±.0186		
13.825	0.137	0.0477±.0203		
13.803	0.190	0.0683±.0229		
13.780	0.245	0.0418±.0232		
13.757	0.298	0.0954±.0260		
13.734	0.353	0.101±.028		
13.712	0.406	0.129±.031		

*Continued*

TABLE VI.D.Continued. For energy = 17.301, the  $ed$  and  $ep$  cross sections per nucleus and the ratio of aluminum-to-deuterium cross sections per nucleon.

$E'$ (GeV)	$W^2$ (GeV <sup>2</sup> )	$\frac{d^2\sigma_d}{d\Omega dE'} (nb/GeV/sr)$	$\frac{d^2\sigma_p}{d\Omega dE'} (nb/GeV/sr)$	$\frac{\sigma_{Al}}{\sigma_d}$
13.689	0.461	0.181±0.032		
13.667	0.514	0.200±0.036		
13.644	0.570	0.260±0.039		
13.622	0.623	0.260±0.041		
13.600	0.675	0.274±0.042		
13.577	0.731	0.336±0.043		
13.555	0.784	0.322±0.047		
13.532	0.839	0.375±0.048		
13.510	0.892	0.397±0.047		
13.487	0.947	0.414±0.050		
13.465	1.000	0.425±0.050		
13.442	1.056	0.238±0.047		
13.420	1.109	0.366±0.052		
13.398	1.161	0.382±0.053		
13.375	1.217	0.460±0.058		
13.353	1.270	0.504±0.060		
13.330	1.325	0.581±0.063		
13.308	1.378	0.549±0.070		
13.285	1.433	0.624±0.071		
13.263	1.486	0.729±0.078		
13.241	1.539	0.671±0.080		
13.218	1.594	0.703±0.084		
13.196	1.647	0.882±0.090		
13.173	1.703	1.07±0.10		
13.151	1.756	1.07±0.10		
13.128	1.811	0.926±0.095		
13.106	1.864	1.06±0.10		
13.083	1.919	1.28±0.11		
13.061	1.972	1.29±0.11		
13.038	2.025	1.13±0.11		
13.015	2.080	1.29±0.11		
12.993	2.133	1.31±0.11		
12.970	2.189	1.36±0.11		

TABLE VI.E. For energy = 18.476, the  $ed$  and  $ep$  cross sections per nucleus and the ratio of aluminum-to-deuterium cross sections per nucleon.

$E'$ (GeV)	$W^2$ (GeV <sup>2</sup> )	$\frac{d^2\sigma_d}{d\Omega dE'} \text{ (nb/GeV/sr)}$	$\frac{d^2\sigma_p}{d\Omega dE'} \text{ (nb/GeV/sr)}$	$\frac{\sigma_{Al}}{\sigma_d}$
14.880	-0.724	0.00596±.00555		
14.857	-0.670	0.00660±.00462		
14.835	-0.616	0.00848±.00422		
14.813	-0.563	0.00784±.00396		
14.791	-0.509	0.0126±0.0036		
14.768	-0.453	0.00645±.00378		
14.746	-0.399	0.0116±0.0037		
14.724	-0.345	0.00965±.00301		
14.702	-0.292	0.0182±0.0031		
14.680	-0.238	0.0165±0.0026		
14.658	-0.184	0.0193±0.0026		
14.636	-0.131	0.0265±0.0031		
14.614	-0.077	0.0258±0.0031		1.92±1.65
14.592	-0.023	0.0299±0.0028		
14.569	0.033	0.0364±0.0031		
14.547	0.087	0.0368±0.0031		
14.525	0.140	0.0502±0.0038		
14.503	0.194	0.0562±0.0035		1.87±0.62
14.481	0.248	0.0613±0.0039		
14.459	0.302	0.0762±0.0038		
14.437	0.355	0.0841±0.0040		
14.415	0.409	0.0981±0.0042		
14.393	0.463	0.107±0.004		1.52±0.24
14.370	0.519	0.116±0.004		
14.348	0.573	0.137±0.005		
14.326	0.626	0.156±0.005		
14.304	0.680	0.181±0.006		
14.282	0.734	0.194±0.006		1.13±0.12
14.260	0.787	0.216±0.007		
14.238	0.841	0.213±0.006		
14.216	0.895	0.224±0.006		
14.194	0.949	0.231±0.006		
14.171	1.005	0.253±0.008		1.09±0.10
14.148	1.058	0.253±0.007		
14.126	1.112	0.263±0.008	0.004±0.009	
14.104	1.166	0.265±0.008	0.031±0.008	
14.082	1.219	0.287±0.008	0.037±0.009	
14.060	1.273	0.300±0.009	0.062±0.010	0.97±0.10
14.038	1.327	0.304±0.009	0.106±0.012	
14.016	1.381	0.374±0.010	0.154±0.014	

*Continued*

TABLE VI.E. Continued. For energy = 18.476, the  $ed$  and  $ep$  cross sections per nucleus and the ratio of aluminum-to-deuterium cross sections per nucleon.

$E'$ (GeV)	$W^2$ (GeV <sup>2</sup> )	$\frac{d^2\sigma_d}{d\Omega dE'} (nb/GeV/sr)$	$\frac{d^2\sigma_p}{d\Omega dE'} (nb/GeV/sr)$	$\frac{\sigma_{Al}}{\sigma_d}$
13.994	1.434	0.381±0.014	0.173±0.015	
13.971	1.490	0.405±0.012	0.195±0.013	
13.949	1.544	0.426±0.014	0.229±0.015	1.00±0.09
13.927	1.598	0.442±0.013	0.232±0.014	
13.905	1.652	0.466±0.013	0.283±0.017	
13.883	1.705	0.482±0.016	0.308±0.016	
13.861	1.759	0.561±0.020	0.324±0.022	
13.839	1.813	0.597±0.019	0.360±0.018	0.98±0.09
13.817	1.866	0.648±0.020	0.351±0.017	
13.794	1.923	0.689±0.021	0.417±0.020	
13.772	1.976	0.732±0.028	0.414±0.020	
13.750	2.030	0.801±0.030	0.482±0.023	0.98±0.10
13.728	2.084	0.853±0.033	0.552±0.026	1.14±0.30
13.704	2.142		0.614±0.031	
13.682	2.196		0.841±0.039	
13.660	2.250		0.857±0.045	
13.638	2.303		0.838±0.040	
13.616	2.357		0.761±0.039	
13.594	2.411		0.675±0.038	
13.572	2.465		0.690±0.040	
13.549	2.521		0.624±0.042	
13.527	2.574		0.720±0.040	
13.505	2.628		0.847±0.053	
13.483	2.682		0.904±0.051	
13.461	2.736		1.05±0.07	
13.438	2.789		1.19±0.08	

TABLE VI.F. For energy = 20.999, the  $ed$  and  $ep$  cross sections per nucleus and the ratio of aluminum-to-deuterium cross sections per nucleon.

$E'$ (GeV)	$W^2$ (GeV <sup>2</sup> )	$\frac{d^2\sigma_d}{d\Omega dE'} (nb/GeV/sr)$	$\frac{d^2\sigma_p}{d\Omega dE'} (nb/GeV/sr)$	$\frac{\sigma_{Al}}{\sigma_d}$
16.391	-0.932	0.00087±0.00142		
16.366	-0.869	0.00239±0.00171		
16.341	-0.806	0.00291±0.00177		
16.316	-0.743	0.00362±0.00165		
16.291	-0.680	0.00453±0.00267		
16.266	-0.617	0.00401±0.00229		
16.241	-0.554	0.00804±0.00191		16.41±19.06
16.216	-0.491	0.00938±0.00159		
16.191	-0.428	0.00851±0.00169		
16.166	-0.365	0.00602±0.00121		
16.141	-0.302	0.00906±0.00135		2.20±2.05
16.116	-0.239	0.0101±0.0011		
16.091	-0.176	0.0107±0.0011		
16.066	-0.113	0.0132±0.0012		
16.041	-0.050	0.0132±0.0015		
16.016	0.013	0.0177±0.0014		2.18±0.84
15.991	0.076	0.0182±0.0014		
15.966	0.139	0.0186±0.0013		
15.941	0.201	0.0256±0.0017		
15.916	0.264	0.0272±0.0018		
15.890	0.330	0.0284±0.0016		2.58±0.36
15.865	0.393	0.0325±0.0015		
15.840	0.456	0.0403±0.0017		
15.815	0.519	0.0474±0.0019		
15.790	0.582	0.0485±0.0020		
15.764	0.645	0.0547±0.0020		1.56±0.19
15.739	0.708	0.0642±0.0021		
15.714	0.771	0.0697±0.0030		
15.689	0.834	0.0742±0.0023		
15.664	0.896	0.0832±0.0026		
15.639	0.959	0.0792±0.0023		1.34±0.18
15.614	1.022	0.0884±0.0026		
15.589	1.085	0.0953±0.0029		
15.564	1.148	0.0991±0.0028	0.0048±0.0034	
15.539	1.211	0.108±0.003	0.001±0.003	
15.514	1.274	0.118±0.004	0.013±0.003	1.29±0.21
15.489	1.337	0.119±0.003	0.019±0.004	
15.464	1.400	0.124±0.004	0.031±0.004	
15.439	1.463	0.146±0.004	0.040±0.005	
15.414	1.526	0.154±0.004	0.059±0.005	

*Continued*

TABLE VI.F.Continued. For energy = 20.999, the  $ed$  and  $ep$  cross sections per nucleus and the ratio of aluminum-to-deuterium cross sections per nucleon.

$E'$ (GeV)	$W^2$ (GeV <sup>2</sup> )	$\frac{d^2\sigma_d}{d\Omega dE'} (nb/GeV/sr)$	$\frac{d^2\sigma_p}{d\Omega dE'} (nb/GeV/sr)$	$\frac{\sigma_{Al}}{\sigma_d}$
15.389	1.589	0.166±0.005	0.071±0.005	1.05±0.18
15.364	1.652	0.180±0.005	0.089±0.007	
15.339	1.715	0.200±0.005	0.093±0.006	
15.314	1.778	0.203±0.006	0.100±0.006	
15.289	1.841	0.222±0.006	0.108±0.007	
15.264	1.904	0.261±0.008	0.125±0.008	1.07±0.14
15.239	1.967	0.280±0.010	0.149±0.007	
15.214	2.030	0.312±0.008	0.160±0.008	
15.189	2.093	0.293±0.009	0.175±0.009	
15.164	2.155	0.328±0.010	0.216±0.010	1.04±0.20
15.139	2.218	0.338±0.014	0.302±0.014	
15.114	2.281	0.354±0.015	0.313±0.015	0.96±0.21
15.089	2.344		0.302±0.014	
15.064	2.407		0.270±0.012	
15.039	2.470		0.267±0.014	
15.013	2.533		0.273±0.016	
14.988	2.596		0.289±0.016	
14.963	2.659		0.285±0.015	
14.938	2.722		0.363±0.017	
14.913	2.785		0.433±0.020	
14.888	2.848		0.449±0.021	
14.863	2.911		0.535±0.027	
14.838	2.974		0.562±0.033	
14.813	3.037		0.520±0.031	

TABLE VII. Elastic Cross section ratios  $\sigma_n^{\text{el}}/\sigma_p^{\text{el}}$  and statistical errors extracted using the Monte Carlo method, and various models of the deuteron wave functions. The probability of having a Fermi momentum greater than 300 MeV/c is shown in parenthesis. The fit was to the range  $0.4 \leq W^2 \leq 1.5 \text{ GeV}^2$ . The  $\chi^2/\text{degree of freedom}$  is also shown.

Deuteron Potential	$Q^2 = 2.5$		$Q^2 = 4.0$		$Q^2 = 6.0$		$Q^2 = 8.0$	
	$\sigma_n/\sigma_p$	$\chi^2$	$\sigma_n/\sigma_p$	$\chi^2$	$\sigma_n/\sigma_p$	$\chi^2$	$\sigma_n/\sigma_p$	$\chi^2$
Holland-Machleidt 2 (2%)	$0.35 \pm 0.02$	3.3	$0.35 \pm 0.01$	0.8	$0.35 \pm 0.01$	0.4	$0.19 \pm 0.04$	0.6
Holland-Machleidt 3 (3%)	$0.38 \pm 0.02$	2.4	$0.37 \pm 0.02$	1.0	$0.37 \pm 0.02$	0.4	$0.23 \pm 0.03$	0.4
Reid Soft Core (4%)	$0.40 \pm 0.01$	1.3	$0.38 \pm 0.01$	0.5	$0.39 \pm 0.02$	0.4	$0.18 \pm 0.03$	0.3
⊗ Modified Reid Soft Core (2%)	$0.34 \pm 0.01$	0.8	$0.36 \pm 0.01$	0.6	$0.37 \pm 0.02$	0.4	$0.21 \pm 0.04$	0.5
Modified Reid Soft Core (4%)	$0.39 \pm 0.01$	2.1	$0.38 \pm 0.01$	0.5	$0.38 \pm 0.01$	0.3	$0.19 \pm 0.04$	0.7
L-F 4.7% d state (4%)	$0.36 \pm 0.02$		$0.29 \pm 0.02$		$0.32 \pm 0.02$		$0.09 \pm 0.04$	
Average	0.37		0.37		0.37		0.20	

TABLE VIII. Values for  $\sigma_n^{\text{el}}/\sigma_p^{\text{el}}$  using the analytic  $y$ -scaling method. The range of values at the bottom includes only models with  $\chi^2 \leq 2.5$  for all  $Q^2$ .

Deuteron Potential	Coefficients		$Q^2 = 2.5$		$Q^2 = 4.0$		$Q^2 = 6.0$		$Q^2 = 8.0$		$Q^2 = 10.0$	
	$c_1$	$c_2$	$\sigma_n/\sigma_p$	$\chi^2$								
LF7.2	0.0	0.0	0.411	2.7	0.407	1.7	0.432	2.3	0.296	1.1	0.182	1.4
REID	0.0	0.0	0.401	3.1	0.408	2.0	0.462	3.1	0.368	1.3	0.334	1.2
PARIS	0.0	0.0	0.398	2.9	0.412	2.0	0.480	3.5	0.405	1.5	0.412	1.5
BONN	0.0	0.0	0.392	2.9	0.416	2.1	0.505	4.1	0.460	2.0	0.528	2.1
PARIS	1.0	0.0	0.347	1.6	0.356	1.6	0.402	2.0	0.299	1.1	0.244	1.2
PARIS	1.5	0.0	0.322	1.4	0.328	1.5	0.366	1.6	0.251	1.1	0.169	1.2
PARIS	1.5	1.5	0.316	1.4	0.320	1.5	0.349	1.5	0.222	1.1	0.145	1.2
PARIS	1.0	2.0	0.338	1.5	0.342	1.5	0.376	1.7	0.232	1.1	0.164	1.2
LF7.2	1.5	1.5	0.323	1.3	0.297	1.4	0.262	1.7	0.048	2.3	-0.229	4.1
REID	1.5	1.5	0.318	1.4	0.311	1.5	0.318	1.4	0.206	1.1	-0.005	1.9
BONN	1.5	1.5	0.313	1.4	0.332	1.6	0.394	1.9	0.312	1.2	0.270	1.4
Range $\sigma_n/\sigma_p$ (good $\chi^2$ ):			0.313–0.347		0.310–0.356		0.318–0.402		0.206–0.312		0.145–0.270	

TABLE IX. The ratios of elastic electron-neutron to elastic electron-proton cross sections. The model dependence is mostly the theoretical uncertainty of the deuteron wave function.

$Q^2$ (GeV/c) <sup>2</sup>	$\sigma_n^{\text{el}}/\sigma_p^{\text{el}}$	Statistical Error	Systematic Error	Model Dependence
2.5	0.35	$\pm 0.01$	$\pm 0.03$	$\pm 0.03$
4.0	0.35	$\pm 0.01$	$\pm 0.03$	$\pm 0.03$
6.0	0.37	$\pm 0.02$	$\pm 0.03$	$\pm 0.04$
8.0	0.24	$\pm 0.04$	$\pm 0.03$	$\pm 0.05$
10.0	0.20	$\pm 0.05$	$\pm 0.03$	$\pm 0.08$

TABLE X. The inelastic-elastic connection for deuterium. Predictions of the elastic form factor  $A_d$  from measurements of the structure function  $W_2$  near threshold. The predicted values of  $A$  come from the measured values of  $W_2$  and the assumption that  $W_2/A_d$  is independent of  $Q^2$ .

$W_d - M_d$	$2.5 < Q^2 < 4$	$Q^2 = 6$		$Q^2 = 8$ (This Experiment)	
	$W_2/A_d$ (average)	$W_2 \times 10^{-7}$ (measured)	$A \times 10^{-9}$ (predicted)	$W_2 \times 10^{-7}$ (measured)	$A \times 10^{-9}$ (predicted)
0.04	$55 \pm 5$	$1.5 \pm 0.9$	$2.7 \pm 1.7$	-	-
0.10	$105 \pm 10$	$2.3 \pm 0.9$	$2.2 \pm 0.9$	-	-
0.14	$160 \pm 15$	$4.1 \pm 1.0$	$2.6 \pm 0.7$	-	-
0.20	$275 \pm 25$	$8.8 \pm 1.6$	$3.2 \pm 0.7$	$0.7 \pm 0.4$	$0.25 \pm 0.15$
Average Predicted			$2.7 \pm 0.4$		$0.25 \pm 0.15$

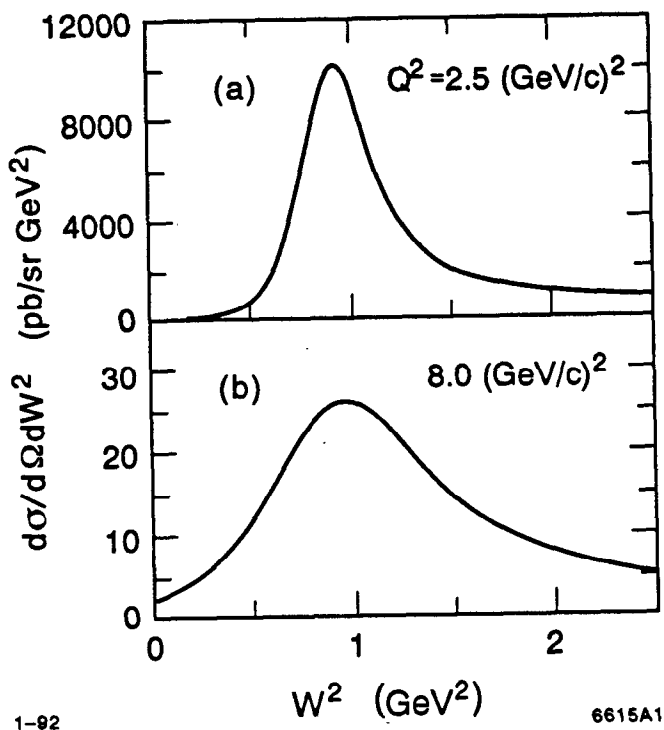


Fig. 1

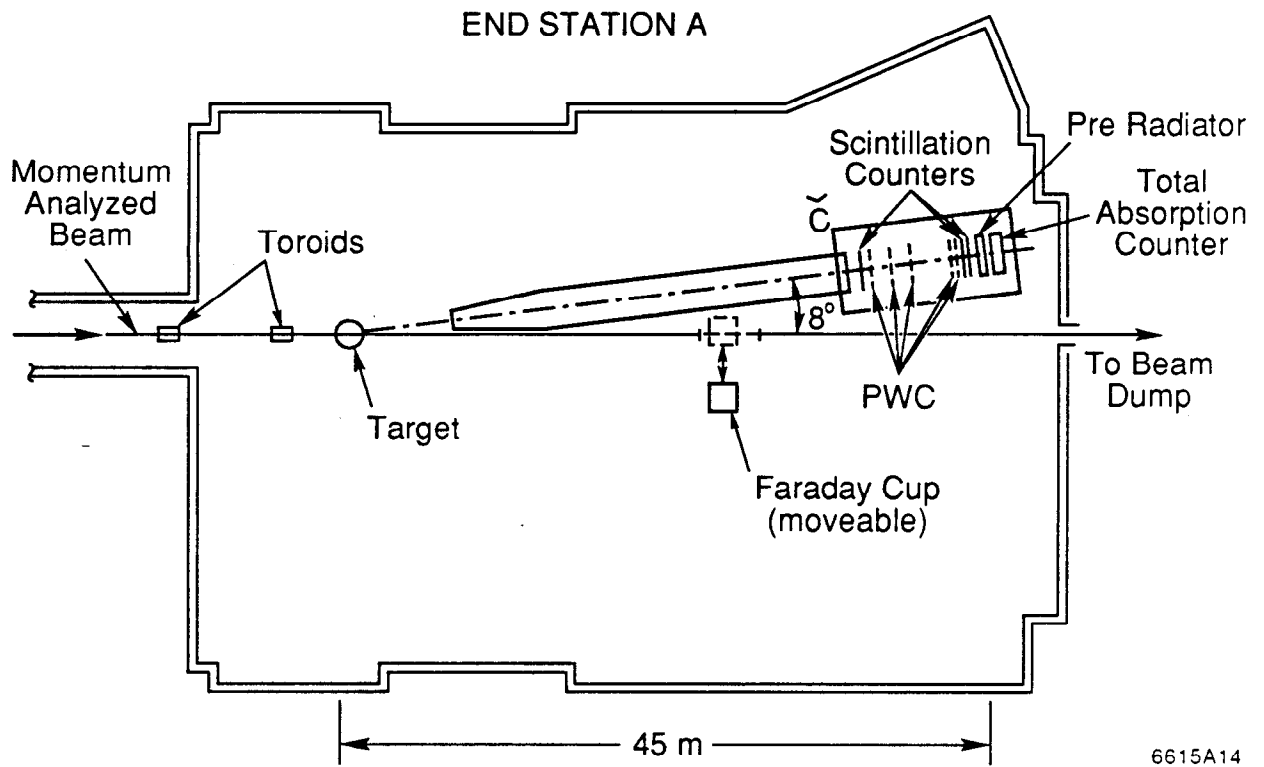


Fig. 2

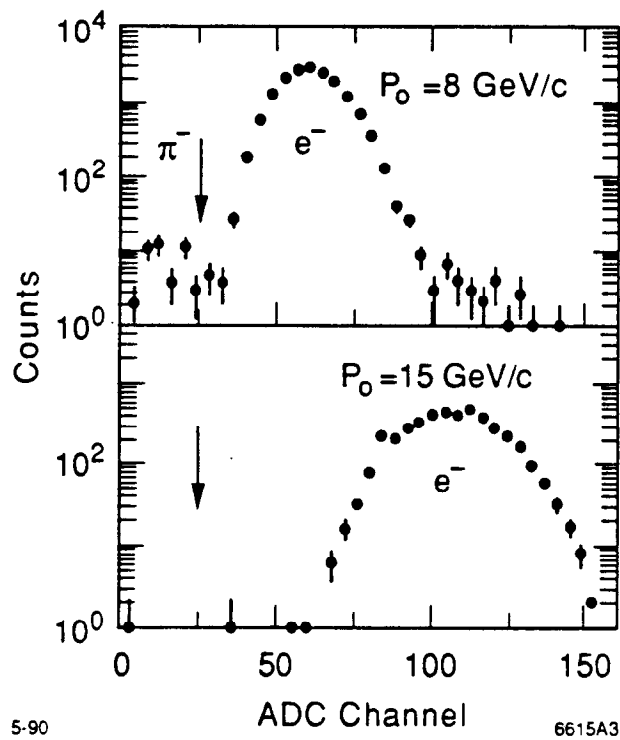


Fig. 3

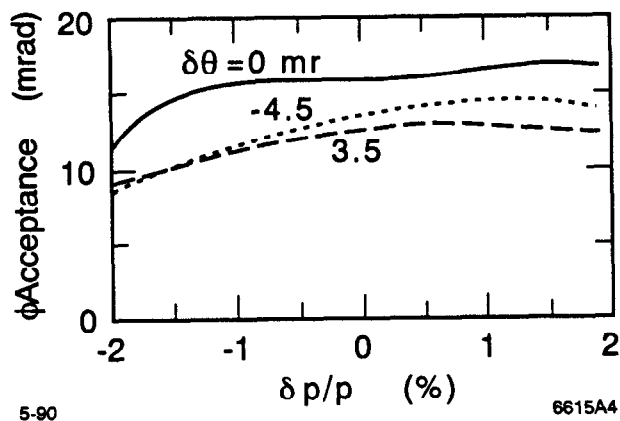


Fig. 4

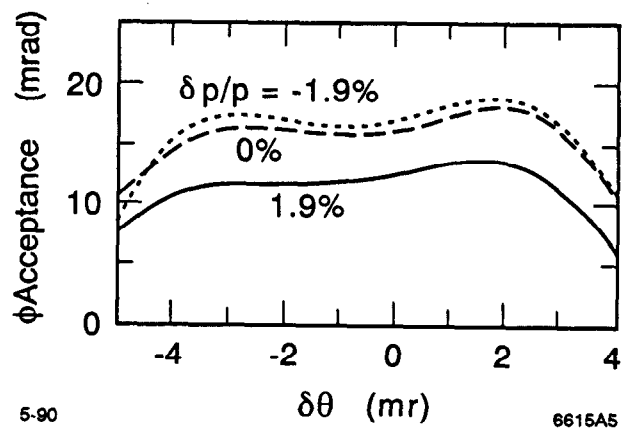
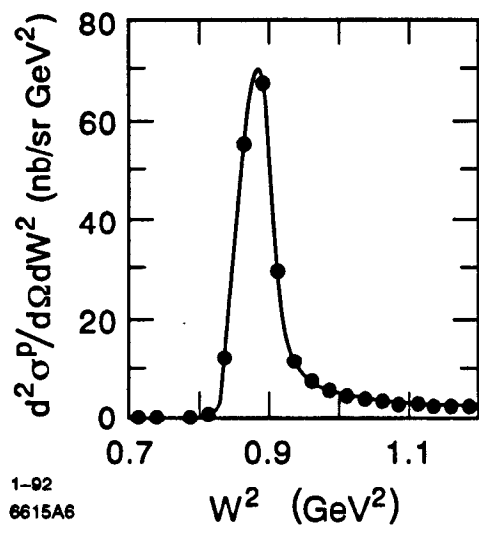


Fig. 5



1-62  
8615A6

Fig. 6

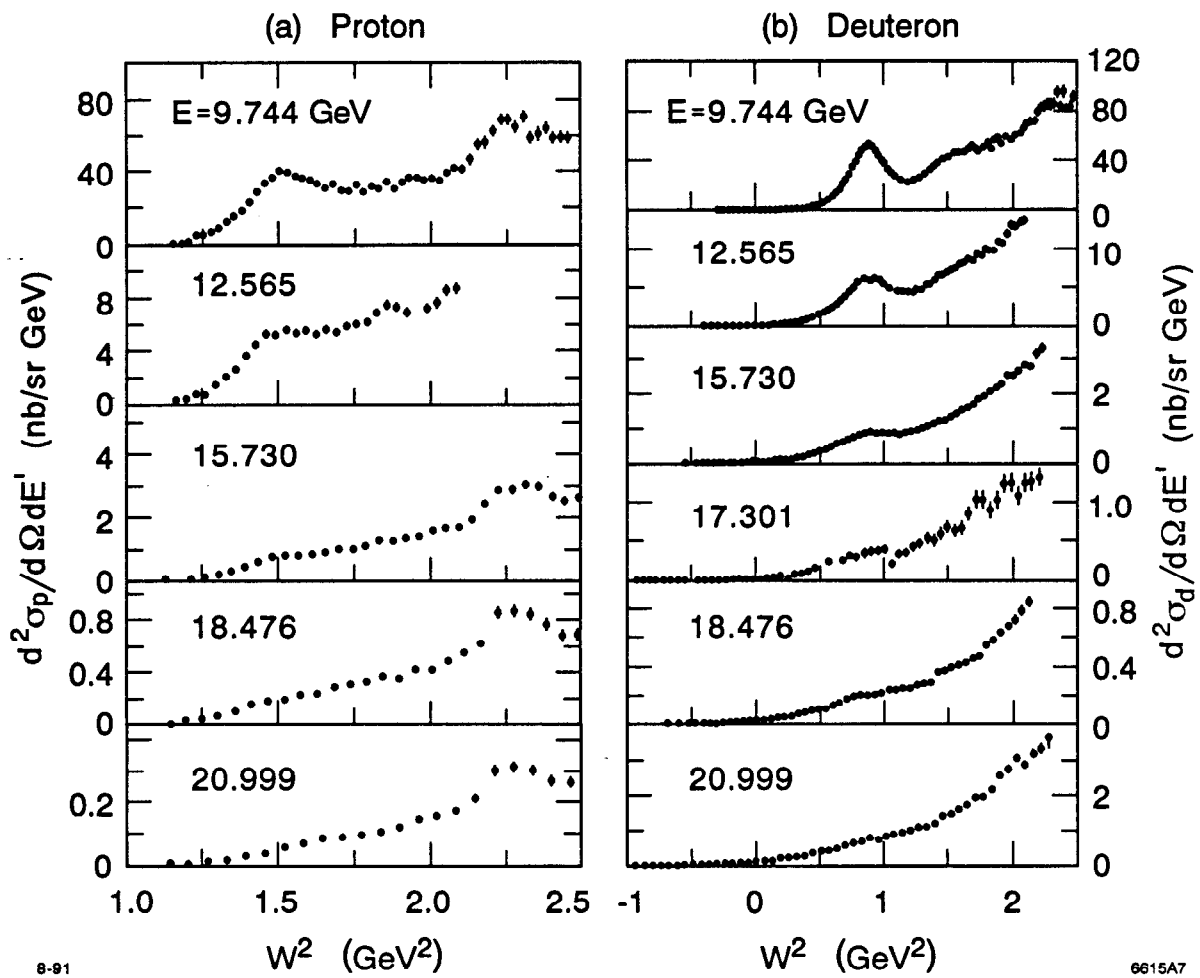


Fig. 7

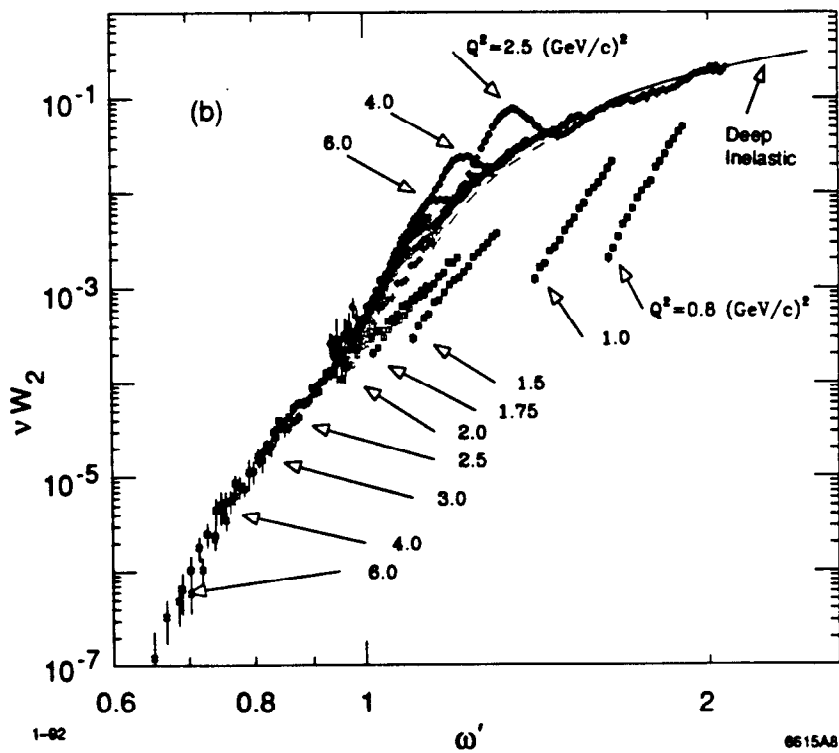
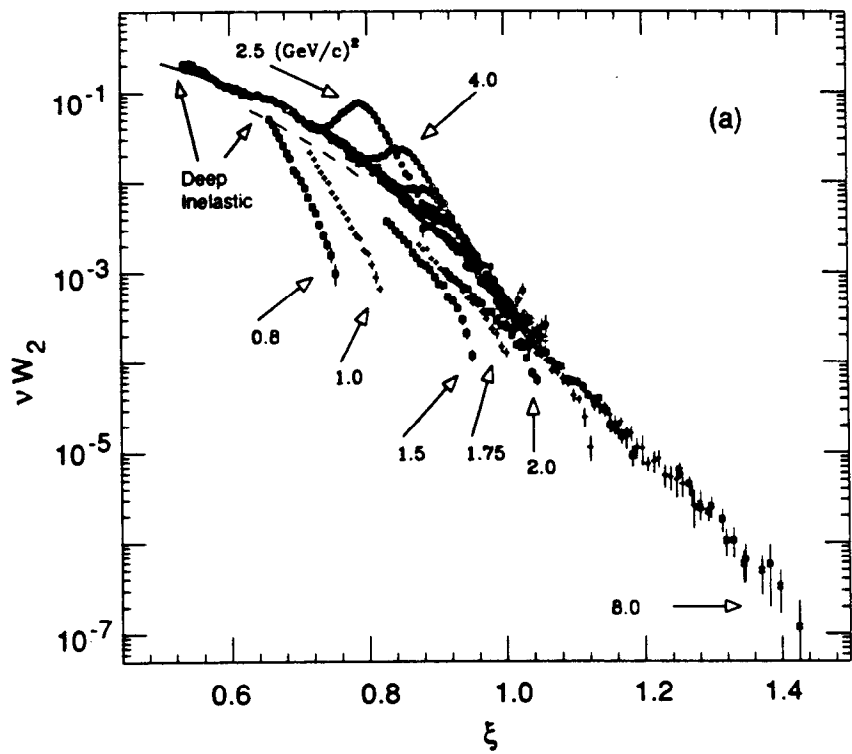


Fig. 8

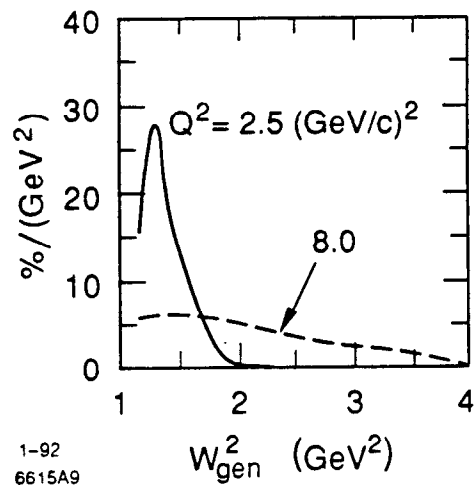


Fig. 9

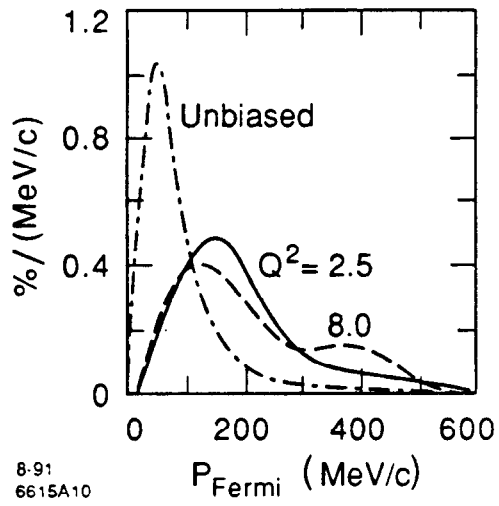


Fig. 10

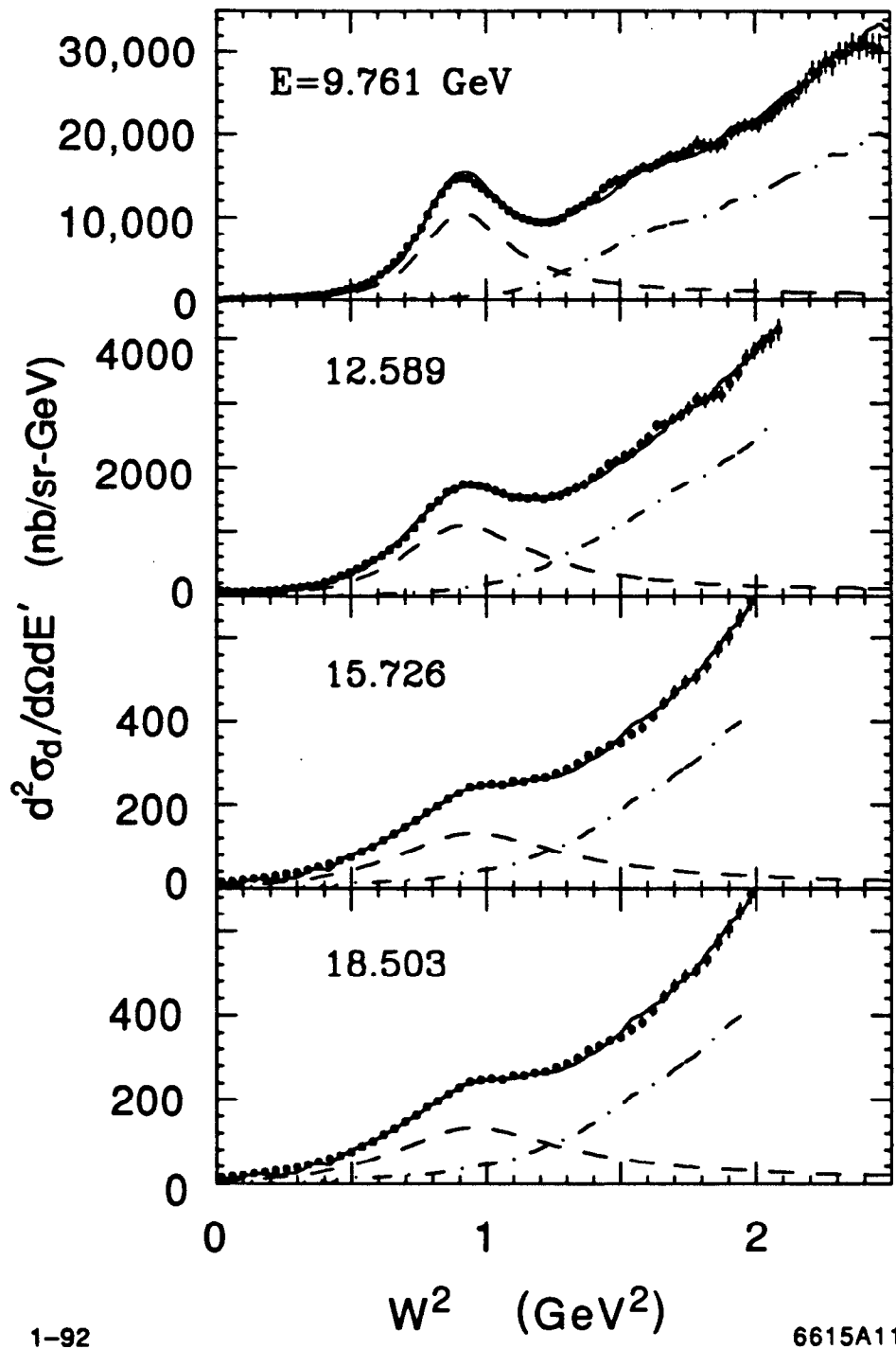


Fig. 11

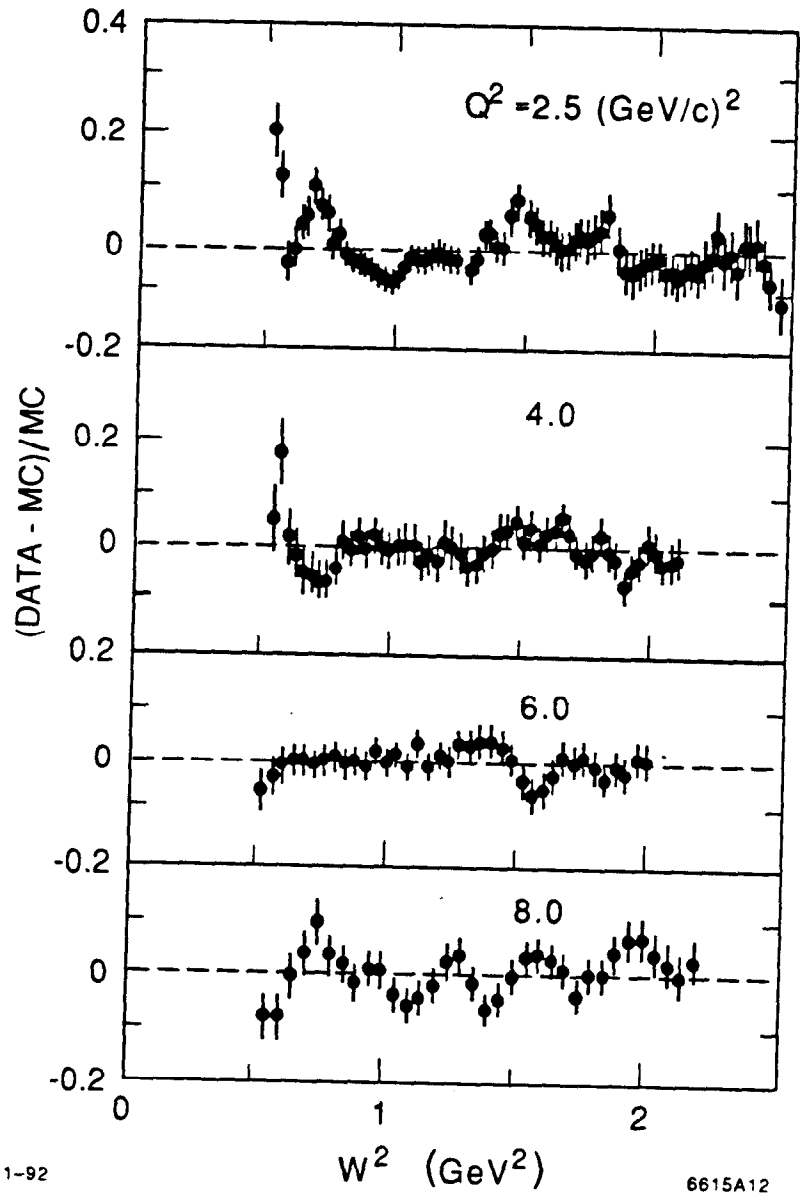
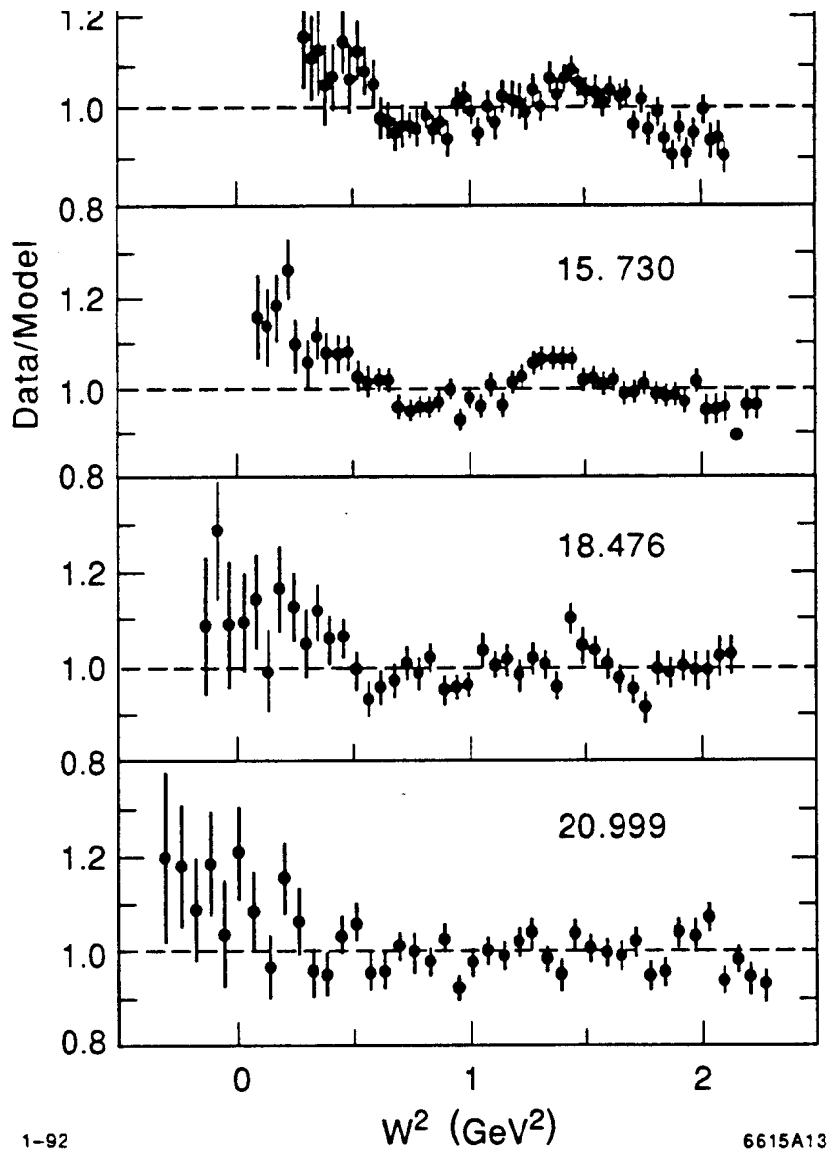


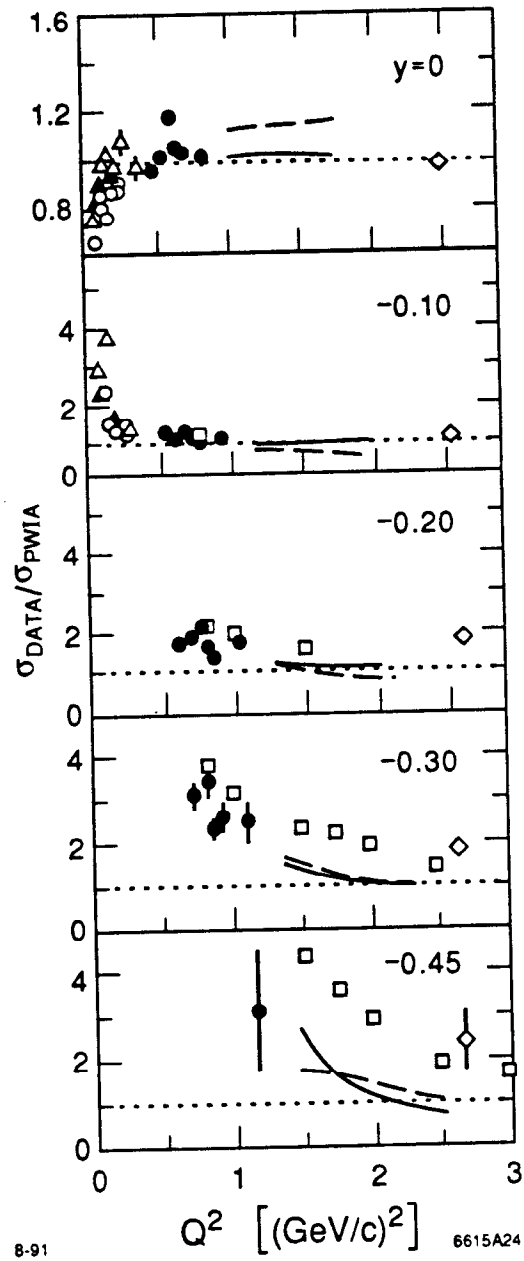
Fig. 12



1-92

6615A13

Fig. 13



8-91

6615A24

Fig. 14

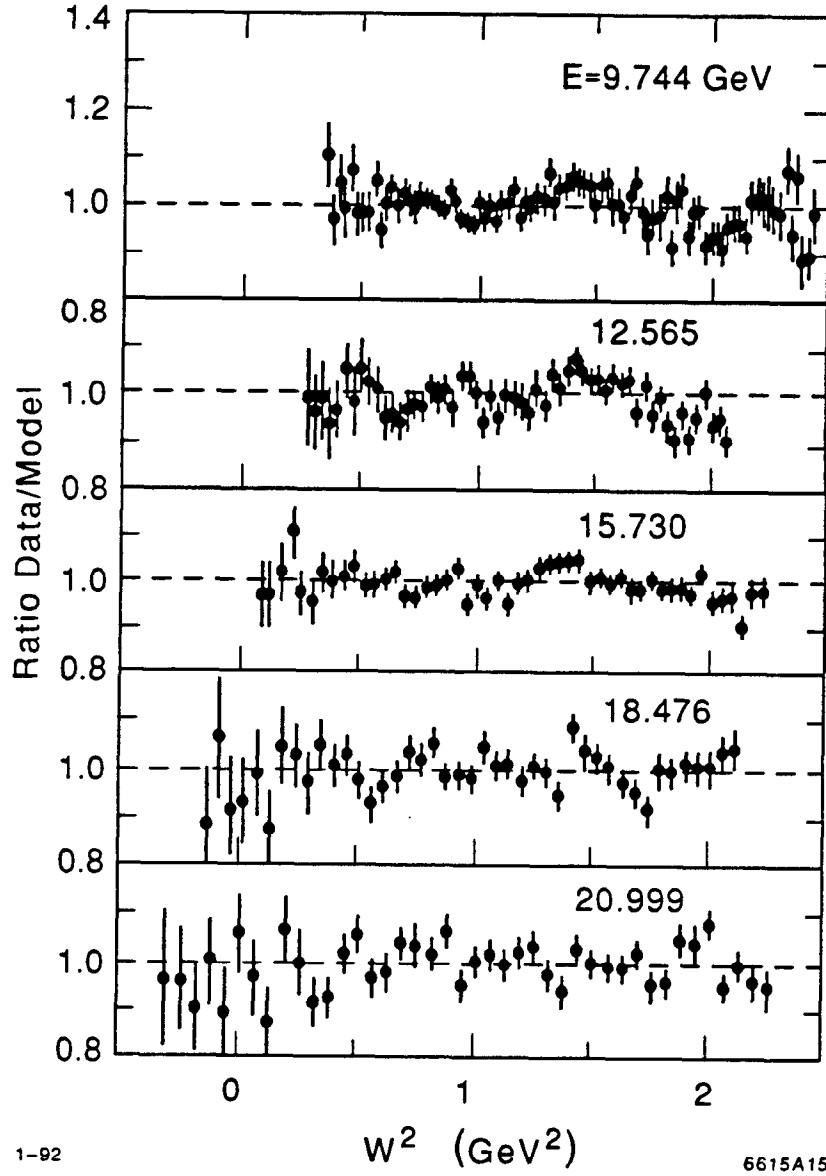


Fig. 15

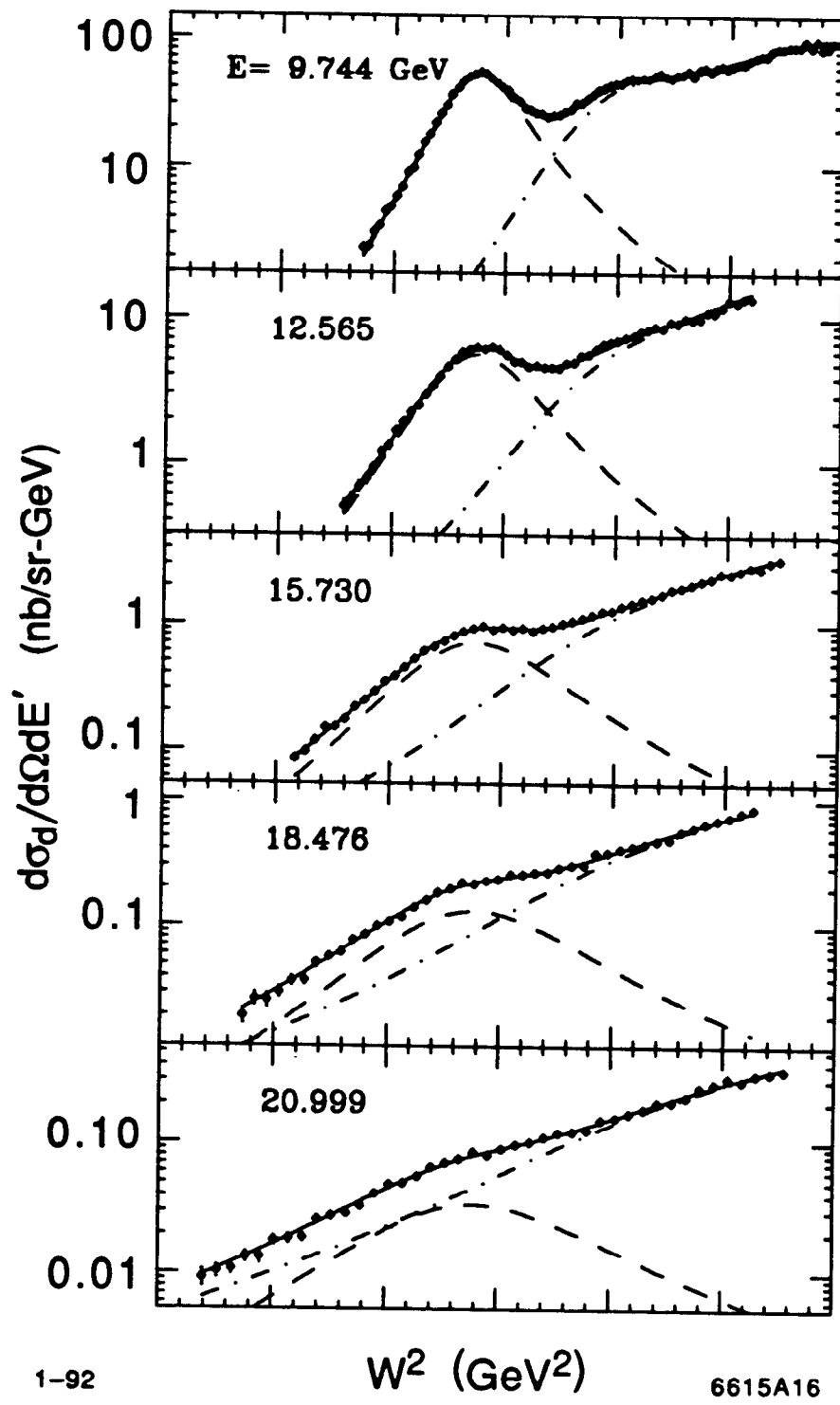


Fig. 16

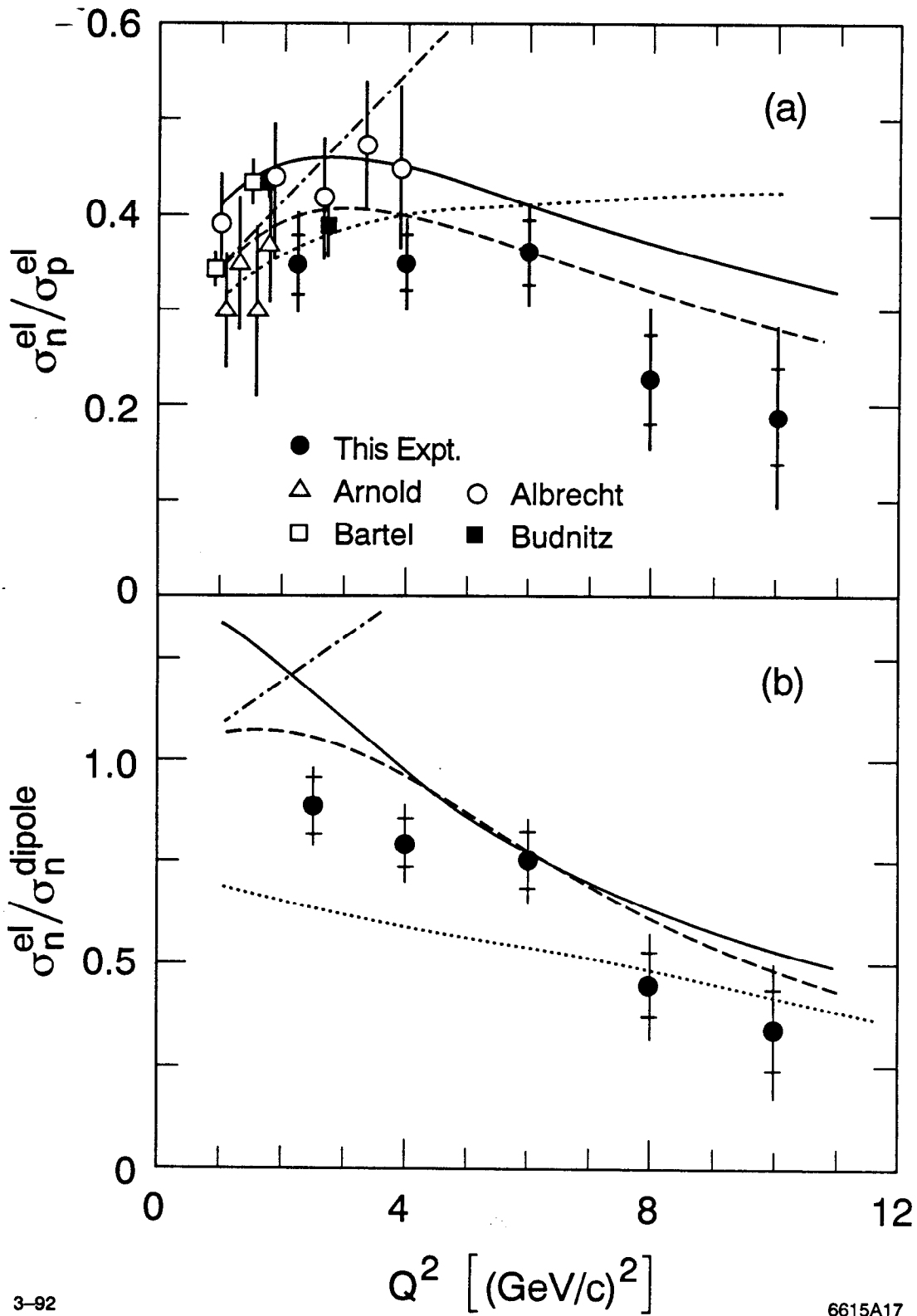
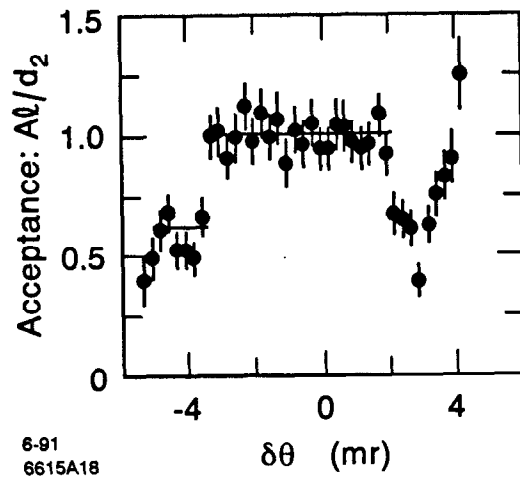


Fig. 17



6-91  
6615A18

Fig. 18

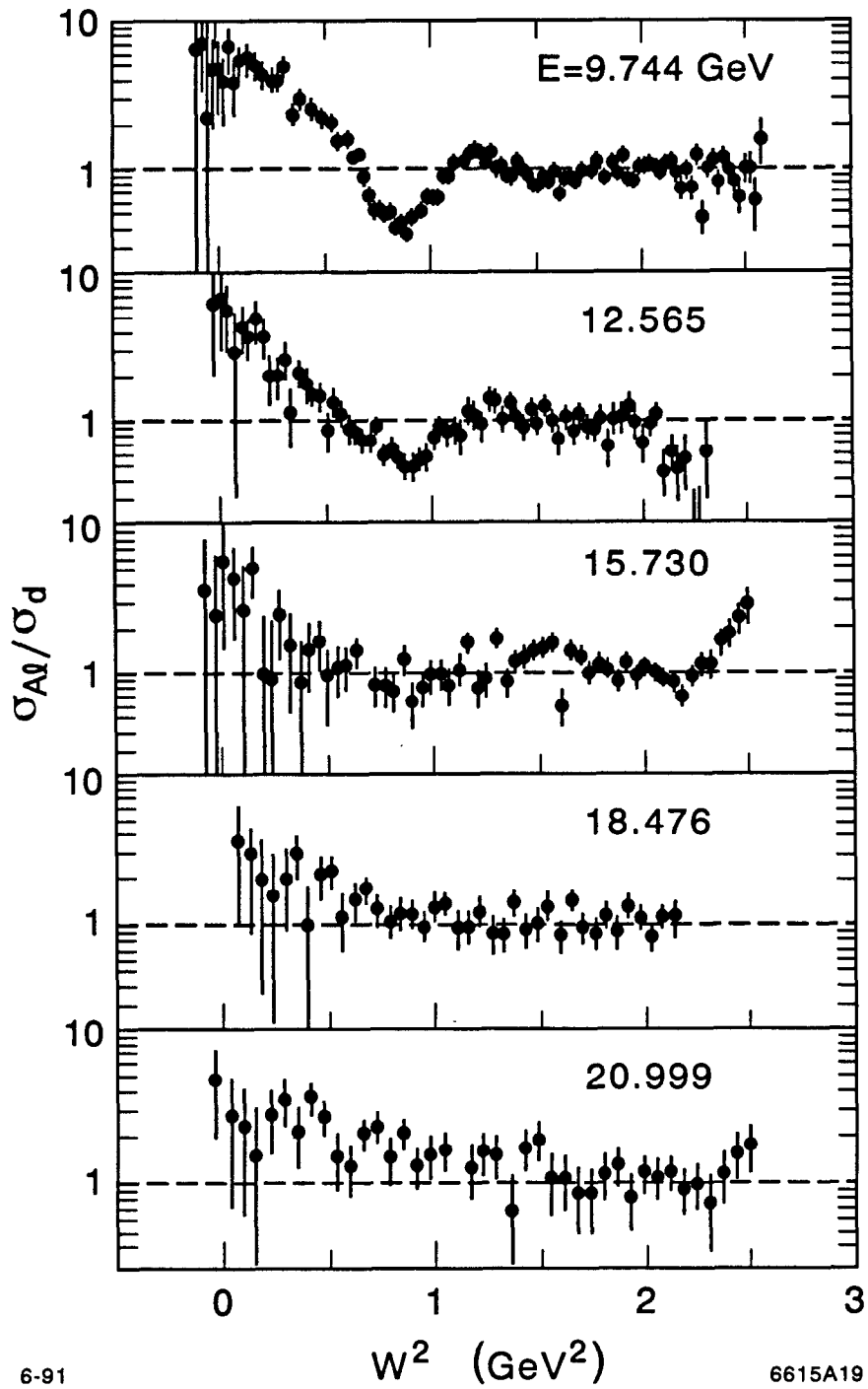


Fig. 19

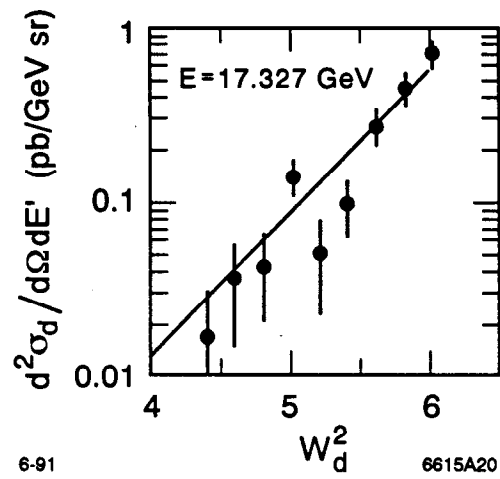


Fig. 20

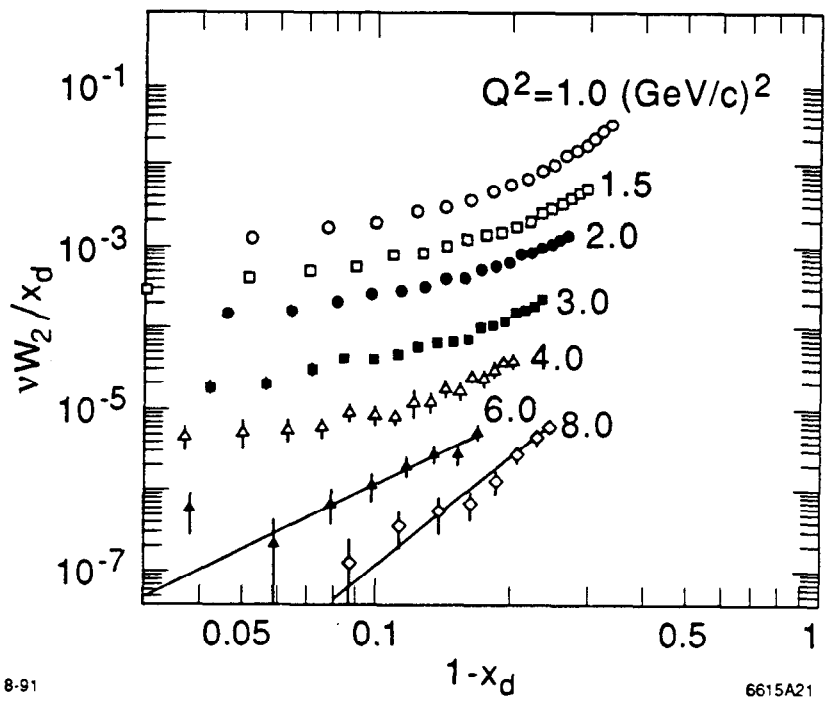


Fig. 21

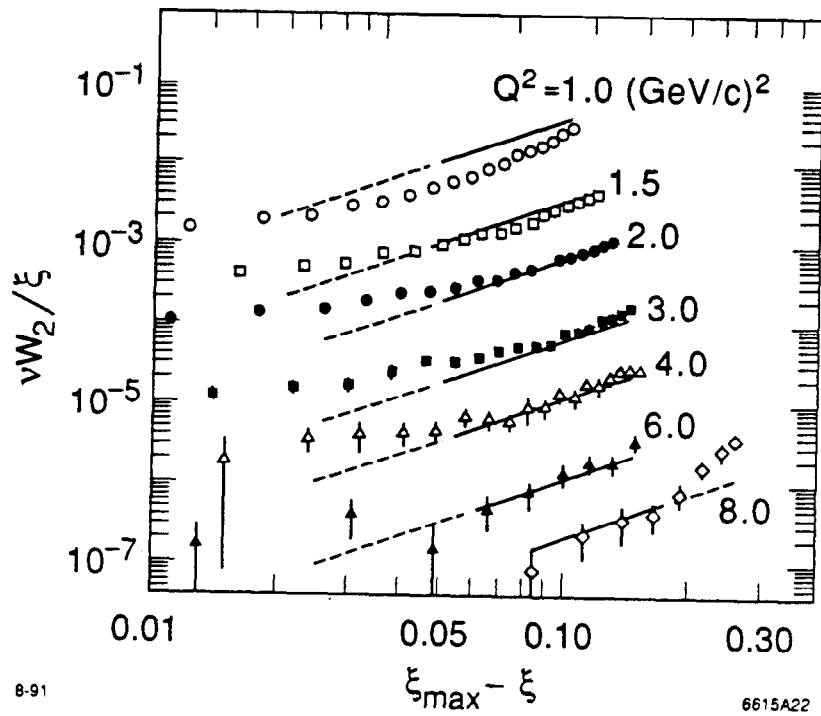


Fig. 22

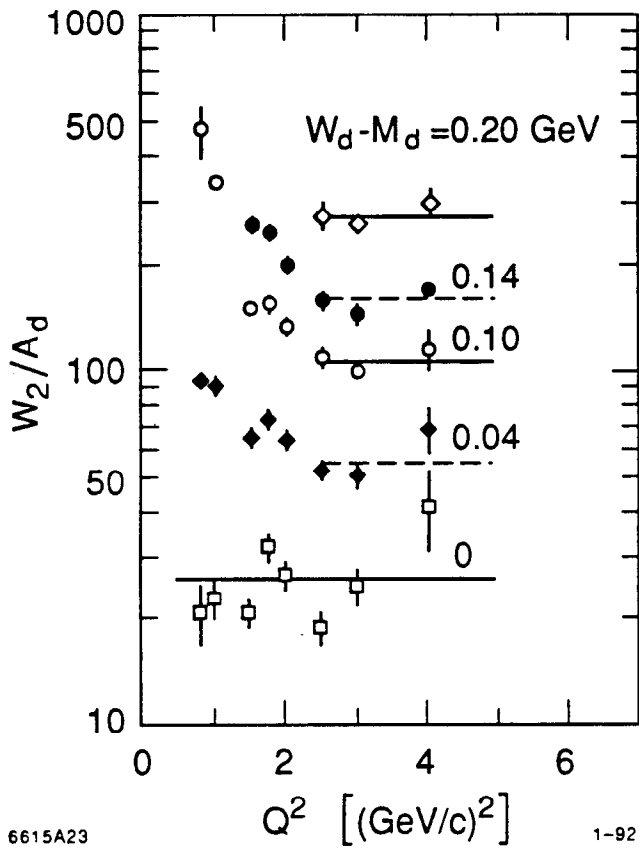


Fig. 23